Figure #	Figure title One sentence only	Filename This should be the name the file is saved as when it is uploaded to our system. Please include the file extension. i.e.: *Smith_ED_Fig1.jpg*	Figure Legend If you are citing a reference for the first time in these legends, please include all new references in the main text Methods References section, and carry on the numbering from the main References section of the paper. If your paper does not have a Methods section, include all new references at the end of the main Reference list.
Extended Data Fig. 1	Selection criteria for the integrated single-cell analysis and gating strategies	ED_Fig1.tif	**a,** Violin plots depicting single-cell expression levels for *BCL6*, *CXCR5* and *FOXP3* transcripts (left panel) in tumor-infiltrating $CD4^+$ T cells of an exemplary dataset[63]; dotted lines indicate threshold used for defining positive cells. The scatter plot (right panel) shows expression levels of *BCL6* and *CXCR5* transcripts in *FOXP3*-expressing *CD4*$^+$ T cells **b**, Gating strategy (surface panel) to sort tumor-infiltrating T_{REG} ($LIN^-CD45^+CD3^+CD4^+CXCR5^-CD127^-CD25^+$) and T_{FR} ($LIN^-CD45^+CD3^+CD4^+CXCR5^+GITR^+$) cells is shown in the representative FACS plots. **c**, Gating strategy (intracellular panel) to identify tumor-infiltrating T_{REG} ($LIN^-CD45^+CD3^+CD4^+CXCR5^-FOXP3^+BCL\text{-}6^-$) and T_{FR} ($LIN^-CD45^+CD3^+CD4^+BCL\text{-}6^+FOXP3^+$) cells is shown in the representative FACS plots. **d**, Representative immunohistochemistry staining for one of the ten NSCLC patients in (**Fig. 1d-i**) is shown, PanCK (white), CD4 (light blue), CXCR5 (yellow), CD20 (magenta) FOXP3 (green) and BCL-6 (red), scale bars are 25μm.
Extended Data Fig. 2	Transcriptome analysis of murine T_{FR} cells and characterization of T_{FR} cells in murine tumors.	ED_Fig2.tif	**a**, Schematic of immunization model in which mice were immunized intraperitoneally (*i.p.*) with Ovalbumin in complete Freund's adjuvant, Ovalbumin in Monophosphoryl Lipid A or mock PBS. **b**, tSNE plot of T_{EFF} ($CD19^-CD45^+CD3^+CD4^+CXCR5^-GITR^-CD25^-CD62L^-$

			$CD44^+$), T_{REG} ($CD19^-CD45^+CD3^+CD4^+CXCR5^-GITR^+CD25^+$), T_{FH} ($CD19^-CD45^+CD3^+CD4^+CXCR5^+GITR^-$) and T_{FR} ($CD19^-CD45^+CD3^+CD4^+CXCR5^+GITR^+$). Each symbol represents data from an individual mouse sample (n=9 for T_{EFF}, n=11 for T_{REG}, n=11 for T_{FH}, n=11 for T_{FR}) that passed quality controls. **c**, Euler diagrams show the overlap of differentially expressed genes (left, upregulated in T_{FR}, right, downregulated in T_{FR}) in T_{FR} cells compared to the indicated cell types. **d**, Heatmap comparing gene signatures of T_{EFF}, T_{REG}, T_{FH} and T_{FR} cells. Depicted are transcripts that change in expression more than 2-fold with a DEseq2 adjusted *P* value of ≤ 0.05. **e**, Log transformed RNA-seq expression values for each of the indicated differentially expressed genes. Each symbol represents an individual sample, data are mean +/- S.E.M. **f**, Representative histogram plot showing MFI of the surface expression of indicated markers in human tumor-infiltrating T_{FR} cells (n=4).
Extended Data Fig. 3	Transcriptome analysis of human tumor-infiltrating T_{FR} cells.	ED_Fig3.tif	**a**, Weighted gene co-expression network analysis (WGCNA) depicted as a Topological Overlap Matrix (TOM) heatmap. It included all genes used in the WGCNA analysis and each row and column correspond to a single gene. Red color indicates the degree of topological overlap. The signed network was generated with bulk RNA-seq data of sorted cells enriched for tumor-infiltrating T_{REG} ($LIN^-CD45^+CD3^+CD4^+CXCR5^-CD127^-CD25^+$) and T_{FR} ($LIN^-CD45^+CD3^+CD4^+CXCR5^+GITR^+$) populations respectively from 10 treatment naïve NSCLC patients (as described in **Fig.2 a-d**). **b**, Spearman correlation analysis of the

			modules identified in (**a)**, depicting module correlation with T_{FR} phenotype. Genes in the pink module are visualized in Gephi, *BCL6* and *FOXP3* are highlighted. **c**, Ingenuity pathway analysis of genes in pink module (**b**). Shown are the top 5 canonical pathways ordered by *P* value. **d**, flow cytometric analysis of the frequency (upper panel, P=0.002 for indicated comparison) and MFI (lower panel, P=0.002 for indicated comparison) of Ki67-expressing cells, representative histogram plots (right panel) for tumor-infiltrating $CD8^+$ T cells, T_{REG} and T_{FR} cells from n=10 NSCLC patient samples (described in **Fig.1 e-f**). **e**, Heatmap comparing gene expression signatures of enriched population of tumor-infiltrating T_{REG} cells (green) and T_{FR} cells (yellow). Depicted are transcripts that change in expression more than 2-fold with an adjusted *P* value of ≤ 0.05. **f**, Weighted gene co-expression network analysis visualized in Gephi, the nodes are colored and sized according to the number of edges (connections), and the edge thickness is proportional to the edge weight (strength of correlation). The top 10 most differentially expressed genes between T_{REG} and T_{FR} cells are highlighted. **g**, flow cytometric analysis of the frequency of tumor-infiltrating $TCF1^+$ T_{REG} and T_{FR} cells from n=5 NSCLC patient samples, P=0.0159). Data are mean +/- S.E.M. Significance for comparisons were computed using two-tailed Wilcoxon matched-pairs signed rank test between T_{REG} and T_{FR} cells (**d**) or two-tailed Mann-Whitney test (**g**).
Extended Data Fig. 4	Cell trajectory	ED_Fig4.tif	**a,** Single-cell pseudo-time trajectory of cells in

	analysis of human T_{REG} and T_{FR} cells from primary tumor tissue and metathesized tumor-infiltrated lymph nodes.		cluster 1 (T_{REG} cells) and cluster 6 (T_{FR} cells) (left) or cells from primary tumor tissue or metastatic tumor-infiltrated lymph nodes (right) constructed using the Monocle3 algorithm. **b**, Normalized gene expression of *IL1R2*, *CCR8*, *TNFRSF9*, *TNFRSF18* and *PDCD1* on pseudotime path as in (**a**).
Extended Data Fig. 5	TCR-seq analysis of tumor-infiltrating T_{REG} and T_{FR} cells.	ED_Fig5.tif	**a**, the pie chart illustrates the mean percentage of T_{FR} clonotypes that were shared with T_{REG} cells (light blue) and non-T_{REG} cells (grey) respectively, from 4 patients with the highest numbers of clonally expanded *FOXP3*-expressing cells from a published single cell RNA-seq dataset[20]. The lower panel plot displays the percentage of T_{FR} clonotypes that overlap with *4-1BB*$^{-}$ or *4-1BB*$^{+}$ tumor-infiltrating T_{REG} cells. **b**, Euler diagram depicting the degree of clonal overlap between T_{REG}, T_{FH} and T_{FR} cells. **c**, Representative TraCer plot of patient 1010[20] depicting all clonally expanded cells, color indicates the type of tumor-infiltrating *CD4*$^{+}$ T cells: non-T_{REG} (grey, *FOXP3*$^{-}$), *4-1BB*$^{-}$ T_{REG} (green), *4-1BB*$^{+}$ T_{REG} (red) and T_{FR} (yellow) cells. **d**, Single-cell pseudo-time trajectory of *4-1BB*$^{-}$, *4-1BB*$^{+}$ T_{REG}, clonally-expanded, TCR-sharing T_{REG} and T_{FR} cells (indicated with colored circles) constructed using the Monocle3 algorithm. **e**, Correlation of Monocle component 1 (x-axis) with the genes commonly unregulated in *4-1BB*$^{+}$ T_{REG}, clonally-expanded, TCR-sharing T_{REG} and T_{FR} cells compared to *4-1BB*$^{-}$ T_{REG} cells (y-axis). The solid line represents LOESS fitting between the shared signature and Monocle component 1. **f**, flow cytometric analysis of the frequency (left panel, P=0.002 for indicated

			comparison), MFI (middle panel, P=0.002 for indicated comparison) for 4-1BB expression in tumor-infiltrating $CD8^+$ T cells, T_{REG} and T_{FR} cells (n=10 treatment naïve NSCLC patients as in Fig.2 a-d). Data are mean +/- S.E.M. Significance for comparisons were computed using two-tailed Wilcoxon matched-pairs signed rank test between T_{REG} and T_{FR} cells.
Extended Data Fig. 6	Characterization of murine T_{FR} cells in immunization and cancer setting.	ED_Fig6.tif	**a**, Gating strategy to identify tumor-infiltrating T_{REG} ($CD19^-CD45^+CD3^+CD4^+BCL\text{-}6^-FOXP3^+$) and T_{FR} ($CD19^-CD45^+CD3^+CD4^+BCL\text{-}6^+FOXP3^+$) cells in B16F10-OVA inoculated mice at d21 (upper panel), shown are representative FACS plots. The FACS plots in the lower panel illustrate intracellular expression of BCL-6 in the indicated cell types (left panel), expression of GITR (middle upper panel), KI-67 (right upper panel), PD-1 (middle lower panel), and CTLA-4 (right lower panel) versus FOXP3 in $CD4^+$ T cells. **b**, Contour plots depicting the expression levels of FOXP3 in the indicated cell populations from (**Fig. 4d)**. **c,** Luminex analysis of supernatants from an *in vitro* proliferation assay (repeat of *in vitro* suppression assay experiment in **Fig. 4g,h**), depicted is the concentration of secreted IFN-γ, IL-2 and TNF. **d**, Flow-cytometric analysis of the frequency of tumor-infiltrating T_{REG} and T_{FR} cells (P=0.0025 in MC38-OVA, n=5 mice for day 14 and n=7 mice for day 21; P=0.0017 in B16F10-OVA, n=10 mice for day 14 and n=6 mice for day 21) in indicated tumor models at indicated time points. Data are mean +/- S.E.M., Significance for comparisons were computed using two-tailed Mann-Whitney test (**d**). Data in **b-d** are representative of

			two independent experiments.
Extended Data Fig. 7	Human T_{FR} cells are responsive to anti-PD-1 therapy.	ED_Fig7.tif	**a**, Heatmap comparing gene signatures of human tumor-infiltrating T_{FR} cells pre- (n=21 patients) and post- (n=26 patients) anti-PD-1 therapy[20]. T_{FR} cells from 5 patients (P2, P3, P12, P15, P20) receiving anti-PD-1 monotherapy were combined. IPA analysis of transcripts (n=98) more highly expressed post anti-PD-1 treatment (right upper panel) and transcripts that overlap with CD28 signaling, ICOS-ICOSL signaling and T cell receptor signaling are highlighted (right lower panel and heatmap). **b-i**, Mice were *s.c.* inoculated with B16F10-OVA cells and treated with tamoxifen (days 5-8 and days 11-14) and anti-PD-1 Abs (day 9). Tumor volume (**b,f**), T_{FR} cell frequencies (**c,** P=n.s., **g,** P=0.035), eGFP cell frequencies (**d,** P=0.0025**, h,** P=0.0012) and FOXP3 frequencies (**e,i**) for n=6 *Foxp3*$^{eGFP\text{-}cre\text{-}ERT2}$ mice, n=7 *Foxp3*$^{eGFP\text{-}cre\text{-}ERT2/wt}$ x *Bcl6*$^{fl/fl}$ mice, n=7 *Foxp3*$^{eGFP\text{-}cre\text{-}ERT2}$ mice and n=5 *Foxp3*$^{eGFP\text{-}cre\text{-}ERT2/wt}$ mice. Data are mean +/- S.E.M., Significance for comparisons were computed using two-tailed Mann-Whitney test (**b-i**). Data in **b-i** are representative of two independent experiments.
Extended Data Fig. 8	Murine T_{FR} cells are depleted by anti-CTLA-4 thereapy	ED_Fig8.tif	**a,b,** *Foxp3*$^{YFPcre/YFPcre}$ *Bcl6*$^{fl/fl}$ (T_{FR} knockout) mice or *Foxp3*$^{YFPcre/YFPcre}$ *Bcl6*$^{+/+}$ control mice were *s.c.* inoculated with B16F10-OVA cells and treated with isotype control or anti-PD-1 Abs at indicated time points, frequency and Ki-67 expression of $CD8^+$ T cells and $CD4^+$ T cells in tumor-draining lymph nodes of mice treated as indicated in, n=7 mice for ctrl+isotype ctrl, n=6 mice for ctrl+anti-PD-1, n=9 mice for the two T_{FR} ko groups. **c**, Mice were *s.c.* inoculated with B16F10-OVA or MC38-OVA cells

			and treated with anti-CTLA-4 Abs at day 10 and day 13. Flow-cytometric analysis of the frequency of tumor-infiltrating T_{REG} and T_{FR} cells, as well as fold depletion of both cell types following anti-CTLA-4 therapy in the B16F10-OVA model (left panel, n=9 mice, P=0.0435) and MC38-OVA model (right panel, n=5 mice, P=0.0079). **d**, Survival curves of an independent cohort of melanoma patients (n=29) stratified into T_{FR}^{hi} (>5.075% of $CD4^+$ cells co-expressing FOXP3 and BCL-6) and T_{FR}^{lo} (<5.075% of cells co-expressing FOXP3 and BCL-6) **e**, IHC analysis of the frequency of $FOXP3^+BCL6^+$ T_{FR} cells with a cutoff (orange line) set to upper limit of normal of 5.075% pertaining to (**Extended Data Fig. 8d**), P=0.0654. **f**, Survival curves of melanoma patients stratified into $CXCR5^{hi}$ (frequency of CXCR5+ cells >8.336%) and $CXCR5^{lo}$ (frequency of CXCR5+ cells <8.336%). **g**, IHC analysis of the frequency of CXCR5+ cells with a cutoff (orange line) set to upper limit of normal of 8.375% pertaining to (**Extended Data Fig. 8f**), P=0.0002. Data are mean +/- S.E.M., Significance for comparisons were computed using two-tailed Mann-Whitney test (**c**,**e,g**) or Mantel-Cox test (**d,f**). Data in (**a-c**) are representative of two independent experiments.

1

Item	Present?	Filename This should be the name the file is saved as when it is uploaded to our system, and should include the file extension. The extension must be .pdf	A brief, numerical description of file contents. i.e.: *Supplementary Figures 1-4, Supplementary Discussion, and Supplementary Tables 1-4.*
Supplementary Information	No		

Reporting Summary	Yes	Reporting summary.pdf
Peer Review Information	Yes	*OFFICE USE ONLY*

Parent Figure or Table	Filename This should be the name the file is saved as when it is uploaded to our system, and should include the file extension. i.e.: *Smith_SourceData_Fig1.xls*, or *Smith_ Unmodified_Gels_Fig1.pdf*	Data description i.e.: Unprocessed Western Blots and/or gels, Statistical Source Data, etc.
Source Data Fig. 1	SourceData_Fig1.xlsx	Source Data Integrated analysis
Source Data Fig. 2	SourceData_Fig2.xlsx	Statistical Source Data
Source Data Fig. 3	SourceData_Fig3.xlsx	Statistical Source Data
Source Data Fig. 4	SourceData_Fig4.xlsx	Statistical Source Data
Source Data Fig. 5	SourceData_Fig5.xlsx	Statistical Source Data
Source Data Fig. 6	SourceData_Fig6.xlsx	Statistical Source Data
Source Data Fig. 7	SourceData_Fig7.xlsx	Statistical Source Data
Source Data Extended Data Fig. 2	SourceData_ED_Fig2.xlsx	Statistical Source Data
Source Data Extended Data Fig. 3	SourceData_ED_Fig3.xlsx	Statistical Source Data
Source Data Extended Data Fig. 5	SourceData_ED_Fig5.xlsx	Statistical Source Data
Source Data Extended Data Fig. 6	SourceData_ED_Fig6.xlsx	Statistical Source Data
Source Data Extended Data Fig. 7	SourceData_ED_Fig7.xlsx	Statistical Source Data
Source Data Extended Data Fig. 8	SourceData_ED_Fig8.xlsx	Statistical Source Data

Intratumoral follicular regulatory T cells curtail anti-PD-1 treatment efficacy

Simon Eschweiler[1], James Clarke[1], Ciro Ramírez-Suástegui[1], Bharat Panwar[1], Ariel Madrigal[1], Serena J Chee[2,3,4], Ioannis Karydis[2,4], Edwin Woo[4], Aiman Alzetani[4], Somaia Elsheikh[5,6], C.J. Hanley[2,3], G.J. Thomas[2,3], Peter S Friedmann[7], Tilman Sanchez-Elsner[3,7], Ferhat Ay[1,8], Christian H Ottensmeier[1,2,3,4,10], Pandurangan Vijayanand[1,3,7,9,10,*]

[1]La Jolla Institute for Immunology, La Jolla, CA, USA.

[2]NIHR and CRUK Southampton Experimental Cancer Medicine Center, Faculty of Medicine, University of Southampton, Southampton, UK.

[3]NIHR Southampton Biomedical Research Center, Faculty of Medicine, University of Southampton, Southampton, UK.

[4]Southampton University Hospitals NHS Foundation Trust, Southampton, UK.

[5]Department of Cellular Pathology, Nottingham University Hospital

[6]Division of Cancer and Stem cells, School of Medicine, University of Nottingham

[7]Clinical and Experimental Sciences, University of Southampton, Faculty of Medicine, Southampton UK.

[8]Department of Pediatrics, University of California San Diego, La Jolla, CA, USA

[9]Department of Medicine, University of California San Diego, La Jolla, CA, USA.

[10]These authors jointly directed the work

*Correspondence: vijay@lji.org

Abstract

Immune checkpoint blockade (ICB) has shown remarkable clinical success in boosting anti-tumor immunity. However, the breadth of its cellular targets and specific mode of action remain elusive. We find that tumor-infiltrating T follicular regulatory (T_{FR}) cells were prevalent in tumor tissues of several cancer types. They were primarily located within tertiary lymphoid structures and exhibited superior suppressive capacity and *in vivo* persistence when compared to T_{REG} cells, with whom they shared a clonal and developmental relationship. In syngeneic tumor models, anti-PD-1 treatment increased the number of tumor-infiltrating T_{FR} cells. T_{FR} cell deficiency or depletion of T_{FR} cells with anti-CTLA-4 antibody prior to anti-PD-1 treatment, improved tumor control in mice. Notably, in a cohort of 271 melanoma patients, treatment with anti-CTLA-4 followed by anti-PD-1 at progression was associated with better survival outcomes than monotherapy with anti-PD-1 or anti-CTLA-4, anti-PD-1 followed by anti-CTLA-4 at progression or concomitant combination therapy.

Introduction

An increased density of T regulatory (T_{REG}) cells in tumors has been linked to poor survival outcomes[1]. In secondary lymphoid organs, T_{REG} cells have been shown to differentiate into PD-1 expressing T follicular regulatory cells (T_{FR}) that restrain germinal center responses[2], impede humoral immunity towards self-antigens and display heightened suppressive capacity when compared to T_{REG} cells[3,4]. T_{FR} cells are being characterized by their joint expression of the surface molecules CXCR5 and GITR[2,5], or by their co-expression of the transcription factors FOXP3 and BCL-6[6]. Several studies have demonstrated that, depending on disease context and organ, cells of the T follicular lineage express varying levels of CXCR5 and BCL-6[7,8]. Notably, it has been shown that deletion of CXCR5 expression in FOXP3-expressing cells does not abrogate the development and maintenance of BCL-6$^+$ T_{FR} cells[6], indicating

68 that distinct subsets of T_{FR} cells exist, which not only differ in their expression of CXCR5 and BCL-6, but also in their expression of
69 CD25[9,10].

70 While the role of T follicular helper (T_{FH}) cells, B cells, and tertiary lymphoid structures (TLS) in driving anti-tumor immune
71 responses and responsiveness to anti-PD1 therapy is now beginning to be elucidated[11–14], few studies have examined potential
72 effects of anti-PD-1 therapy on the regulatory T cell compartment. Accordingly, T_{FR} cells, their functional role in cancer, and their
73 responsiveness to ICB have been completely overlooked so far. Based on the well-described functions of T_{FR} cells in secondary
74 lymphoid organs, we hypothesized that T_{FR} cells are likely to be present in the TLS of tumors and modulate immune responses in the
75 tumor microenvironment (TME). Moreover, as T_{FR} cells have a skewed TCR repertoire towards self-antigens and because cancerous
76 cells frequently express self or altered-self antigens, we hypothesized that T_{REG} and T_{FR} cells accumulate in parallel in the TME as a
77 means of effective immune evasion.

78 Herein, we report that T_{FR} cells account for a substantial proportion of tumor-infiltrating $CD4^+$ T cells, and importantly, that
79 they are highly responsive to ICB. We further demonstrate that T_{FR} cells are highly suppressive, are prevalent in multiple different
80 cancer types, and accumulate in tumor tissues over time, likely mediated by their higher proliferative capacity and persistence *in vivo*
81 that is dependent on BCL-6. Depleting T_{FR} cells or blocking their activity with anti-CTLA-4 antibodies prior to anti-PD-1 therapy,
82 improved efficacy of anti-PD-1 treatment in mouse tumor models and was also associated with better survival outcomes in a large
83 cohort of melanoma patients. Finally, we found that T_{FR} cells, but not T_{REG} cells, were enriched within TLS, suggesting that T_{FR} cells
84 might also impair patient survival and impede immunotherapy treatment efficacy by regulating TLS, consistent with their well-
85 described role in secondary lymphoid organs[3,4]. Our findings thus challenge the current clinical practice of unselective administration

of anti-PD-1 therapy, which hence overlooks any possibility for its potential to impede anti-tumor immune responses. By elucidating the functional properties of intratumoral T_{FR} cells and by identifying them as one of the major targets of ICB, we provide critical insights into how anti-CTLA-4 and anti-PD-1 therapies mediate their function and highlight the potential clinical benefit of depleting intratumoral T_{FR} cells prior to initiation of anti-PD1 therapy.

Results

T_{FR} cells are present in multiple cancer types

We integrated 9 published single-cell RNA-seq datasets and performed a meta-analysis of tumor-infiltrating $CD4^+$ T cells (n=25,149) from patients with six different cancer types (**Table 1)**. As expected, *FOXP3*-expressing $CD4^+$ T cells (*i.e.*, T_{REG} cells) clustered distinctly and represented 5-55% of all tumor-infiltrating $CD4^+$ T cells (**Fig. 1a,b**). We found that a substantial proportion (5-30% in all tumor types) of *FOXP3*-expressing $CD4^+$ T cells co-expressed *BCL6* and/or *CXCR5* (**Fig. 1c and Extended Data Fig. 1a**), which encode for markers indicative of cells of a follicular lineage in humans and mice[2,15], and thus represent tumor-infiltrating T_{FR} cells, an important regulatory subset that has not been appreciated so far. We confirmed the presence (~10-20% of all tumor-infiltrating $CD4^+$ T cells) and localization of T_{FR} cells in tumor samples from patients with treatment-naïve early-stage non-small cell lung cancer (NSCLC) by multi-parameter flow cytometry and immunohistochemistry (**Fig.2a-f, Extended Data Fig. 1b-d** and **Table 2**). T_{FR} cells, like T_{REG} cells, maintained surface expression of CD25 and ICOS (**Fig. 2b**). To determine if currently available immunotherapies, like anti-CTLA4 and anti-PD1 therapies, also target tumor-infiltrating T_{FR} cells, we assessed their expression of CTLA-4 and PD-1. Notably, T_{FR} cells expressed the highest levels of CTLA-4 and PD-1 among all tumor infiltrating T cells (**Fig. 2c,d**), suggesting that anti-CTLA-4 can more efficiently target T_{FR} cells, and that anti-PD-1 therapies may inadvertently activate such

suppressive T_{FR} cells. A fraction (~15%) of all tumor-infiltrating $CD4^+$ T cells exhibited a T_{FH} cell phenotype (**Fig. 2a**) that lacked expression of CD25, but expressed ICOS, CTLA-4 and PD-1 (**Fig. 2b-d**). Given the recent findings highlighting the importance of B cells, T_{FH} cells and TLS with regard to heightened anti-tumor immunity, improved patient survival and responsiveness to immunotherapy[11–14], we next assessed the cellular context in which T_{FR} cells exert their function within the TME. Multicolor-immunohistochemistry analyses confirmed the presence of T_{FR} cells in tumor tissues (**Fig. 2e** and **Extended Data Fig. 1d**). Crucially, we found that T_{FR} cells, unlike T_{REG} cells, were predominantly located within TLS (**Fig. 2f**), indicating that T_{FR} cells might inhibit anti-tumor immunity by impeding the function of cells in their vicinity (i.e., of ectopic B and T_{FH} cell responses) or by regulating TLS formation or maintenance.

T_{FR} cells exhibit unique transcriptomic features

As few studies have thoroughly analyzed the transcriptomic features of T_{FR} cells, we first utilized well-established immunization models in mice to gain mechanistic insights into T_{FR} cell function and to assess whether the features identified in human tumor-infiltrating T_{FR} cells are also applicable to murine T_{FR} cells. Immunization with ovalbumin and adjuvant (CFA or MPLA) induced robust T_{FR} responses (**Extended Data Fig. 2a**). Comparative analysis of their transcriptome with that of other T_H subsets showed increased expression of many transcripts specifically in T_{FR} cells (n=84), (**Extended Data Fig. 2b-e** and **Table 3**), and notably the transcripts enriched in T_{REG} cells compared to both T_{FH} and T_{EFF} populations (n=127) were also highly expressed in T_{FR} cells (**Extended Data Fig. 2d,e)**. These include several transcripts (*e.g.*, *Tnfrsf1b*[16], *Lag3*[17], *Tigit*[18], *Batf*[19], and *Il1r2*[1,20]) encoding for products associated with heightened suppressive capacity; *Ccr8*, which was associated with particularly poor clinical outcomes in cancer[1,21], and genes associated with $CD8^+$ T cell dysfunction and survival[22] (*Pdcd1* and *Tox*) (**Extended Data Fig. 2d,e**). The

protein expression levels of some of these molecules, *e.g.,* TNFR2 (encoded by *TNFRSF1B*), LAG3, TIGIT and CCR8, were confirmed in human tumor-infiltrating T_{FR} cells (**Extended Data Fig. 2f**), suggesting suppressive capacity of T_{FR} cells and likely conservation of functional potential across species.

We next performed bulk RNA-seq analyses of enriched populations of T_{REG} ($CD4^+CD25^+CXCR5^-$) and T_{FR} cells ($CD4^+CXCR5^+GITR^+$) (**Extended Data Fig. 1b**) isolated from tumor samples of NSCLC patients (**Table 4**). Weighted gene co-expression network analysis (WGCNA) (**Extended Data Fig. 3a** and **Table 5**) of bulk-sorted human T_{REG} ($CD4^+CD25^+CXCR5^-$) and T_{FR} cells ($CD4^+CXCR5^+GITR^+$) (**Extended Data Fig. 1b**) identified a module (pink) that was positively correlated with the T_{FR} phenotype (**Extended Data Fig. 3b**). Importantly, this module contained both *BCL6* and *FOXP3*, demonstrating the linked expression of these genes, specifically in T_{FR} cells. Ingenuity Pathway Analysis (IPA) of the pink module (**Table 6**) (module positively correlated with T_{FR} phenotype) identified substantial enrichment of genes involved in cell cycle, transcriptional and translational activity and mTOR signaling, indicative of increased T_{FR} cell proliferation and activity (**Extended Data Fig. 3c**). We confirmed that T_{FR} cells indeed showed greater cell proliferation in the TME as evidenced by increased KI-67 staining (**Extended Data Fig. 3d**). Differential gene expression analysis of enriched populations of T_{FR} cells and T_{REG} cells identified over 100 transcripts that were expressed at higher levels in T_{FR} cells (**Extended Data Fig. 3e** and **Table 4**). Co-expression analysis of these differentially expressed transcripts revealed a number of highly correlated novel genes (e.g. *DUSP14, CLP1)*, which may play a role in T_{FR} cell function. Moreover, we identified *TCF7* (encoding TCF-1) as a highly connected hub gene in this transcriptomic network (**Extended Data Fig. 3f**) and confirmed that the proportion of TCF-1-expressing cells was higher in T_{FR} cells compared to T_{REG} cells (**Extended Data Fig. 3g**). Interestingly, TCF-1-expressing $CD8^+$ CTLs have recently been recognized for their ability for self-renewal, stem-like

properties[23,24], and their pivotal role in mediating anti-cancer immune attack induced by anti-PD-1 immunotherapy[25,26], suggesting that TCF-1 expression might confer similar features on T_{FR} cells. Together, these data indicate that intratumoral T_{REG} and T_{FR} cells differ in their molecular profile and demonstrate that T_{FR} cells are highly proliferative in tumor tissue.

Intratumoral T_{REG} and T_{FR} cells are clonally and developmentally related

Recent data demonstrate that tumor-infiltrating T_{REG} cells potently recognize tumor (neo)antigens and, upon antigen-encounter, undergo clonal expansion[27]. Given that antigen-specific activation of T_{REG} cells in the context of viral infection has been implicated in promoting their differentiation into T_{FR} cells *via* TCF-1-mediated induction of BCL-6[28], we hypothesized that tumor-associated antigen (TAA) recognition may also trigger T_{REG} to T_{FR} conversion within the TME. To assess this, we performed combined single-cell RNA-seq and TCR-seq of sorted $CD4^+$ (T_{FH}, T_{REG} and T_{FR}) and $CD8^+$ TILs from primary tumor tissue and tumor-infiltrated lymph nodes of two HNSCC patients (n= 8,722 cells). Unsupervised clustering revealed two distinct *$CD4^+$* T cell clusters (1 and 6) that were enriched for *FOXP3* expression (**Fig. 3a**), and which exhibited distinct transcriptomic signatures (**Fig. 3b** and **Table 7**). Gene set enrichment analysis showed that cells in cluster 6 (yellow) were significantly enriched for follicular (**Fig. 3c**) and T_{FR} cell signatures (**Fig. 3d**), thus characterizing T_{FR} cells, while cells in cluster 1 (green) depict T_{REG} cells. Pathway analysis of the differentially expressed genes (**Fig. 3b**) between T_{FR} and T_{REG} cells showed enrichment for transcripts linked to metabolism, cell activation and co-stimulation (**Fig. 3e**). Moreover, T_{FR} cells expressed higher levels of transcripts liked to T_{FR} function and suppressive capacity (*e.g.*, *CTLA4*, *IL10*, *TGFB1*, *TNFRSF9*, or *IL1R2*), and cell cycle genes (*TOP2A*, *MKI67*) (**Fig. 3f**)**.** Accordingly, although T_{REG} and T_{FR} cells shared clonotypes (**Fig. 3g,h** and **Table 8**), T_{FR} cells were more clonally expanded than T_{REG} cells (**Fig. 3i)**. Importantly, TCR sharing and trajectory analysis of cells in the *FOXP3*-enriched clusters indicate intratumoral conversion of T_{REG}

to T_{FR} cells (**Fig. 3g,h** and **Extended Data Fig. 4a,b**). To further substantiate this notion, we re-analyzed one of the largest single-cell RNA-seq datasets[20] of tumor-infiltrating $CD4^+$ T cells (**Table 9)**, showing that the majority of clonally-expanded T_{FR} clonotypes (~93%) were shared with T_{REG} cells (**Extended Data Fig. 5a,** upper panel), but not T_{FH} cells (**Extended Data Fig. 5b**). Furthermore, T_{REG} cells that shared clonotypes with T_{FR} cells predominantly expressed *4-1BB* (*TNFRSF9*) transcripts (**Extended Data Fig. 5a,** lower panel and **Extended Data Fig. 5c**), implying recent TCR activation[29], and indicative of potential intratumoral conversion of TAA-activated T_{REG} to T_{FR} cells. Trajectory analysis implies that *4-1BB*$^+$ T_{REG} cells (TAA-experienced) and T_{REG} cells sharing TCRs with clonally-expanded T_{FR} cells (purple) depict transitional states during differentiation of T_{REG} cells into T_{FR} cells (**Extended Data Fig. 5d**). Importantly, transcripts linked to cell activation, co-stimulation and suppressive function (**Fig. 3j** and **Table 10**) were expressed at higher levels in *4-1BB*$^+$ T_{REG} cells (red), TCR sharing T_{REG} cells (purple) and clonally-expanded T_{FR} cells (yellow) compared to *4-1BB*$^-$ T_{REG} cells (green), a gene signature that was highly associated with Monocle component 1 (**Fig. 3j and Extended Data Fig. 5e**). When compared to *4-1BB*$^-$ T_{REG} cells, T_{FR} cells and T_{REG} cells on their trajectory to differentiate into T_{FR} cells also showed significant downregulation of *CCR7* and *S1PR1*, genes that encode receptors required for tissue egress, suggesting tissue residency of T_{FR} cells[30] (**Fig. 3j**).

These observations are consistent with a model in which the TME is initially infiltrated by a large and highly diverse pool of bystander (*i.e.*, not TAA-specific) T_{REG} cells, and a smaller pool of TAA-specific T_{REG} clones, which are poised for differentiation into tissue resident T_{FR} cells. This implies that T_{FR} cells comprise a larger proportion of tumor-reactive clones than T_{REG} cells, a notion substantiated by our finding that T_{FR} cells expressed significantly higher levels of 4-1BB than T_{REG} cells (**Extended Data Fig. 5f**) and also by the higher degree of clonal expansion (**Fig. 3i**).

T_{FR} cells exhibit superior suppressive capacity

Next, we assessed frequency, activity and functional responsiveness of T_{FR} cells in murine tumor models. T_{FR} cells ($CD3^+CD4^+BCL\text{-}6^+FOXP3^+$) were present in tumor samples from two syngeneic tumor model systems (B16F10 melanoma and MC38 colorectal tumor cell lines) (**Fig. 4a** and **Extended Data Fig. 6a**), but importantly lacked expression of CXCR5. Notably, recent studies demonstrated that ablation of CXCR5 expression in $FOXP3^+$ T cells did not abrogate the development of $BCL\text{-}6^+$ T_{FR} cells, which still entered the germinal center reaction[6]. Thus, BCL-6 expression in $FOXP3^+$ cells delineates T_{FR} cells even in the absence of CXCR5. Similar to human T_{FR} cells, murine T_{FR} cells exhibited increased proliferative potential, as evidenced by KI-67 expression levels, and increased expression of TCF-1 and 4-1BB compared to T_{REG} cells (**Fig. 4b**). Interestingly, T_{FR} cells also expressed significantly higher levels of the transcription factor TOX (**Fig. 4c**). Given that TOX was recently shown to be essential for the function and survival of TCF-1-expressing $CD8^+$ T cells following chronic antigen-exposure, we speculate that TOX expression in T_{FR} cells may help maintain their superior functionality in the face of sustained stimulation by TAA[31,32].

To experimentally validate that T_{FR} cells are more suppressive than T_{REG} cells, we performed functional assays *in vitro* and *in vivo*. Strikingly, we found that T_{FR} cells inhibited $CD8^+$ T cell proliferation more efficiently than T_{REG} cells (**Fig. 4d-f** and **Extended Data Fig. 6b**), and also reduced their secretion of effector molecules interferon-γ, Interleukin (IL)-2 and Tumor necrosis factor (TNF) more effectively (**Fig. 4g** and **Extended Data Fig. 6c**). Notably, when compared to T_{REG} cells, T_{FR} cells reduced the secretion of interferon-γ by $CD8^+$ T cells ~4–fold, and the secretion of IL-2 and TNF by $CD8^+$ T cells ~2-fold (**Fig. 4h**). These data demonstrate that T_{FR} cells are highly suppressive and imply that they are able to actively diminish the effector functions of $CD8^+$ T cells, even at low cell numbers. Based on these results, we chose to transfer OT-I T cells, either alone or with T_{REG} or T_{FR} cells in a 4:1 ratio, into

198 B16F10-OVA tumor-bearing RAG1 KO recipient mice. While the effect of adoptively transferred T_{REG} cells was negligible, T_{FR} cells
199 substantially inhibited OT-I T cell-mediated tumor rejection (**Fig. 4i**), demonstrating that T_{FR} cells exhibit superior suppressive
200 potential when compared to T_{REG} cells.
201
202 **Intratumoral T_{FR} cells increase over time**
203 To further characterize the properties of intratumoral T_{REG} and T_{FR} cells, we barcoded tumor-infiltrating FOXP3-expressing
204 $CD4^+$ T cells from individual B16F10-OVA tumor-bearing FOXP3-RFP reporter mice from an early (day 11) and a late (day 18) tumor
205 developmental stage, and subjected them to 10x-based single-cell RNA-sequencing. UMAP analysis identified 5 clusters (**Fig. 5a**)
206 with distinct transcriptomic signatures (**Fig. 5b)**, implying the existence of multiple T_{REG} cell subsets within tumor tissues. Importantly,
207 all clusters were present at both time points, but only cells in cluster 2 were enriched in d18 (later time point) tumor samples (**Fig.**
208 **5a,c**). GSEA showed that cells in cluster 2 were significantly enriched for signatures linked to T cell activation (**Fig. 5d**), T_{FH} and T_{FR}
209 cells (**Fig. 5e**), and hence depict activated T_{FR} cells, suggesting that T_{FR} cells increase in tumors over time. Single-cell differential
210 gene expression analysis highlighted profound differences in the transcriptome of T_{FR} cells (cluster 2) and T_{REG} cells in the other
211 clusters (**Fig. 5f**). In line with our previous data (**Extended Data Fig. 2d,e**), T_{FR} cells exhibited increased expression of T_{FR} signature
212 genes (i.e. *Pdcd1, Tnfrsf18*), genes involved in TCR signaling (*Cd3g, Cd3d, Cd3e, Lck*) as well as of several genes which are
213 associated with heightened functionality *(i.e. Tnfrsf1b*[16,33]*, Tigit*[18]*, Tnfrsf9*[29]*, Lag3*[17]*, Tox*[32]) or suppressive capacity (*Tgfb1*) indicative
214 of an activated phenotype and further suggestive of their suppressive potential. T_{FR} cells also showed a significant decrease in the
215 expression of genes that encode receptors required for tissue egress (*S1pr1, Klf2*), suggesting that they may possess greater tumor-
216 residency properties compared to other T_{REG} subsets. (**Fig. 5f,g**). As in our previous analyses (**Extended Data Fig. 5a,c**), we found

substantial clonal overlap between T_{REG} and T_{FR} cells (**Fig. 5h**). Finally, cell-trajectory analysis points to a developmental path from cells in cluster 0, which exhibit features of naïve recirculating T_{REG} cells (**Fig. 5g**), to T_{FR} cells (**Fig. 5i**), further corroborating our previous data (**Extended Data Fig. 4a** and **Extended Data Fig. 5d**). Together, these data, besides highlighting the transcriptional properties of T_{FR} cells, establish a clonal and developmental relationship between T_{REG} and T_{FR} cells and are further indicative of intratumoral T_{REG} to T_{FR} conversion. Based on these findings, we performed a time course experiment which confirmed that the proportion of intratumoral T_{FR} cells, but not T_{REG} cells, increased with tumor progression (**Extended Data Fig. 6d**), likely reflective of ongoing T_{REG} to T_{FR} conversion and higher proliferative potential of T_{FR} cells. Murine tumor-infiltrating T_{FR} cells also showed higher expression of CTLA-4 and PD-1 when compared to T_{REG} cells (**Fig. 5j**), implying that such murine tumor models would be appropriate to test the hypothesis that anti-PD1 therapy increases the numbers and/or function of highly suppressive T_{FR} cells, inducing a profoundly immunosuppressive tumor milieu. Since PD-$1^{-/-}$ mice exhibit increased levels of T_{FR} cells in secondary lymphoid organs[5], we reasoned that PD-1 signaling is likely to restrain expansion of T_{FR} cells.

T_{FR} cells are responsive to anti-PD-1 therapy

Anti-PD-1 monotherapy resulted in a significant increase in the frequency of T_{FR} cells in both MC38 and B16F10 tumor models (**Fig. 6a** and **Table 11**), suggesting that tumor-infiltrating T_{REG} (and T_{FR} cells) are highly responsive to blockade of PD-1 signaling, potentially reducing their activation threshold and thus facilitating increased proliferation and differentiation into T_{FR} cells. By re-analyzing published single-cell RNA-seq data from patients receiving anti-PD-1 therapy, we found that tumor-infiltrating T_{FR} cells from post-treatment samples compared to pre-treatment samples were enriched for transcripts linked to T cell activation and co-stimulation (**Extended Data Fig. 7a** and **Table 12**). Together, these data suggest that engagement of suppressive T_{FR} cells by anti-

PD1 therapy is likely to diminish its anti-tumor efficacy. To uncouple the effects of T_{REG} and T_{FR} cells on anti-tumor immunity and anti-PD-1 treatment efficacy, we utilized a genetic knockdown system, in which T_{FR} cells can be selectively depleted. Tamoxifen-induced depletion of T_{FR} cells in female heterozygous *Foxp3*$^{eGFP\text{-}cre\text{-}ERT2cre/wt}$ x *Bcl6*$^{fl/fl}$ mice[34] prior to initiation of anti-PD-1 therapy, significantly decreased tumor growth, demonstrating that T_{FR} cells curtail anti-PD-1 treatment efficacy (**Extended Data Fig. 7b**). In this system, half of the FOXP3$^+$ cells should express the *Foxp3*$^{eGFP\text{-}cre\text{-}ERT2}$ allele (eGFP$^+$ and BCL-6-deficient) due to random X chromosome inactivation. Surprisingly however, while we found a decrease in T_{FR} cells (**Extended Data Fig. 7c**), we observed a near total loss of BCL-6-deficient eGFP$^+$ T_{REG} cells in the TME (**Extended Data Fig. 7d**), while the frequency of FOXP3-expressing cells only decreased slightly **Extended Data Fig. 7e**). These findings were further corroborated in a control experiment by assessing tumor growth and cell frequencies in homozygous *Foxp3*$^{eGFP\text{-}cre\text{-}ERT2}$ and heterozygous *Foxp3*$^{eGFP\text{-}cre\text{-}ERT2/wt}$ (BCL-6-sufficient) mice (**Extended Data Fig. 7f-i**). Crucially, these data imply that even a partial T_{FR} cell depletion decreases tumor growth, and that BCL-6 expression in FOXP3$^+$ cells is likely to be required for their intratumoral persistence. These findings raise several distinct conclusions explaining for the accumulation of eGFP$^-$FOXP3$^+$ cells; (i) BCL-6-deficiency affects trafficking of T_{REG} cells into tumor tissue. (ii) lack of BCL-6 expression precludes adoption of a tissue-residency program, and (iii) BCL-6-deficient T_{REG} cells are being outcompeted by their BCL-6-sufficient counterparts. While we cannot formally rule out any of these possibilities, the latter hypothesis is supported by our prior observations of increased proliferative potential, as well as higher expression of TOX and TCF-1 by BCL-6$^+$ T_{FR} cells compared to BCL-6$^-$ T_{REG} cells.

To assess the functional importance of T_{FR} cells in tumor development and to further corroborate that T_{FR} cells impair anti-PD-1 treatment efficacy, we utilized T_{FR} cell-deficient *Foxp3*$^{YFP\text{-}cre}$ x *Bcl6*$^{fl/fl}$ mice[35]. We chose to test this hypothesis in the B16F10-OVA

melanoma model as it is known to be refractory to anti-PD-1 therapy[36]. Accordingly, anti-PD-1 treatment in control mice did not impact tumor growth (**Fig. 6b**). Conversely, in T_{FR} knockout mice, we found a trend towards lower tumor volume (isotype control), which was significantly reduced by anti-PD-1 therapy (**Fig. 6b**), demonstrating that T_{FR} cells inhibit the efficacy of anti-PD-1 immunotherapy. To further explore potential impacts of a lack of T_{FR} cells on anti-tumor immunity in this setting, we also assessed tumor-draining axillary and inguinal lymph nodes. The frequency and proliferative capacity of $CD8^+$ and $CD4^+$ T cells in tdLN were similar between the treatment groups (**Extended Data Fig. 8a,b**). However, akin to our previous findings demonstrating that T_{FR} cells can inhibit $CD8^+$ T cell activity and cytokine secretion (**Fig.4 g,h**), we found that T_{FR} cell deficiency results in increased granzyme B expression in $CD8^+$ T cells (**Fig. 6c**). Together, these data suggest that T_{FR} cells inhibit $CD8^+$ T cell activity in tumor-draining lymph nodes.

To experimentally validate that T_{FR} cells have greater *in vivo* persistence in tumor tissue, we performed a competition assay, where we co-transferred $FOXP3^+eGFP^+$ cells from *Foxp3*^{eGFP} mice (capable of producing BCL-6) and $FOXP3^+YFP^+$ cells from *Foxp3*$^{YFP\text{-}cre}$ x *Bcl6*$^{fl/fl}$ mice (incapable of producing BCL-6) in a 1:1 ratio. Strikingly, $FOXP3^+YFP^+$ cells failed to accumulate in the spleen and TME (**Fig. 6d**) of B16F10-OVA tumor-bearing Rag1$^{-/-}$ mice, demonstrating that $FOXP3^+BCL\text{-}6^+$ cells (T_{FR} cells) are better suited to survive in the TME. Importantly, the transferred tumor-infiltrating $FOXP3^+$ cells expressed significantly higher levels of BCL-6 when compared to pre-transfer levels, indicative of T_{REG} to T_{FR} conversion either inside or outside of the tumor (**Fig. 6e**), corroborating our previous findings (**Extended Data Fig. 5a-c**). As it is contentious whether the *Foxp3*-YFPcre allele should be considered hypomorphic[37,38], which might account at least partially for the observed phenotype, we performed a control experiment with $FOXP3^+YFP^+$ cells from *Foxp3*$^{YFP\text{-}cre}$ mice (no *Bcl6* floxed allele). In this control setting, we found that $FOXP3^+YFP^+$ cells did

accumulate in spleen and TME, albeit at slightly lower levels than FOXP3^{+}RFP^{+} cells from *Foxp3*^{RFP} mice (**Fig. 6f**). While these data imply that the knock-in of the YFP-Cre fusion protein might impact FOXP3 expression or cell functionality, they importantly verify that BCL-6 expression is required for the persistence of FOXP3-expressing cells in tumor.

Sequential ICB is beneficial in melanoma patients

As our findings demonstrated that T_{FR} cells curtail the efficacy of anti-PD-1 therapy (**Fig. 6b** and **Extended Data Fig. 7b**), we reasoned that it may be necessary to deplete T_{FR} cells in the tumor prior to initiating anti-PD1 therapy to overcome the suppressive milieu induced by anti-PD-1-mediated increase in T_{FR} cells. Anti-CTLA-4 treatment is believed to deplete intratumoral T_{REG} cells via antibody-dependent cellular cytotoxicity[39]. Given that tumor-infiltrating T_{FR} cells expressed higher levels of CTLA-4 than T_{REG} cells in both human and mouse, we hypothesized that T_{FR} cells should be more efficiently depleted. Indeed, anti-CTLA-4 monotherapy resulted in greater depletion of T_{FR} cells compared to T_{REG} cells (**Extended Data Fig. 8c**). These data also indicate that immunotherapy drugs elicit immediate effects on target cell populations and rapidly re-shape the cellular composition within the TME. Based on these results and our previous findings, we reasoned that sequential immune checkpoint blockade (ICB) treatment, where T_{FR} cells are initially depleted by anti-CTLA-4, might prove beneficial, as subsequent anti-PD-1 therapy would not activate suppressive cellular targets (T_{FR} cells) but would instead engage CD8^{+} TILs to enhance anti-tumor immune responses. As before, we tested this in the B16F10-OVA melanoma model, which is refractory to anti-PD-1 therapy[36]. As expected, monotherapy with either anti-CTLA-4 or anti-PD-1 antibodies did not impact tumor growth, whereas depletion of T_{FR} cells with anti-CTLA4 followed by anti-PD1 therapy led to a significantly reduced tumor volume (**Fig. 7a**). Consistent with our hypothesis, we found that anti-PD-1 therapy

290 increasingly acts on, and hence elevates the frequency of $CD8^+$ TILs after T_{FR} cells have been depleted by anti-CTLA-4 treatment,
291 and also led to an increase in the frequency of granzyme B^+ $CD8^+$ and $CD4^+$ CTLs (**Fig. 7b**).

292 To test the clinical significance of sequential ICB treatment, we retrospectively assessed the survival outcomes of patients
293 with inoperable melanoma (n=271), who were, based on their treatment regimens, stratified into 5 groups: 1st line anti-CTLA-4, 1st
294 line anti-PD-1, simultaneous combination therapy, sequential therapy with anti-CTLA-4 followed by anti-PD-1 at progression and vice
295 versa. Sequential treatment with anti-CTLA-4 followed by anti-PD-1 was associated with better long-term overall survival (OS)
296 outcomes when compared to the 4 other groups (P<0.001) (**Fig. 7c** and **Table 13**). It has to be noted though that patients receiving
297 simultaneous ICB therapy exhibited a more advanced disease prior to treatment initiation (higher proportion with AJCC 8 stage M1c
298 and M1d (n=75) than patients on 1st line anti-PD-1 (n=70) or 1st line anti-CTLA-4 (n=52), **(Fig. 7d,e** and **Table 13**), likely contributing
299 to their poor OS outcomes. However, the advantageous effect of anti-CTLA-4 followed by anti-PD-1 therapy was preserved in
300 patients with M1a/b and M1c/d, respectively (**Fig. 7d,e**), indicating that this treatment regimen is clinically beneficial even in patients
301 with very poor prognosis. Differences in BRAF status did not affect ICB treatment outcomes (**Fig. 7f**). Our outcome data for patients
302 receiving 1st line anti-CTLA-4 appear to be superior to those in a recently published study[40], but are however not directly comparable,
303 as the proportions of patients going on to receive 2nd line anti-PD-1 treatment was significantly lower in that trial (43% vs 63%).
304 Crucially and in-line with our findings in mouse models (**Fig. 7a,b**), when compared to monotherapy with anti-PD1, sequential
305 treatment with anti-CTLA-4 (likely to deplete T_{FR} cells in the tumor or to block their activity) followed by anti-PD-1 was associated with
306 significantly better survival outcomes (P=0.0003) (**Fig. 7c-e**).

In an independent cohort of patients with melanoma (n=29), who received anti-PD1 treatment, we observed poor survival outcomes in patients with a higher proportion of $CD4^+$ T cells co-expressing FOXP3 and BCL-6 ($BCL\text{-}6^+$ T_{FR} cells) in tumor (**Extended Data Fig. 8d**), and also noticed a trend towards a higher frequency of T_{FR} cells ($BCL6^+FOXP3^+CD4^+$ T cells) in non-responders compared to responders to anti-PD-1 treatment (**Extended Data Fig. 8e**). A lower frequency of $CXCR5^+$ cells (**Extended Data Fig. 8f**), a surrogate marker for the abundance of TLS, was also associated with poor survival outcomes (**Extended Data Fig. 8g**), consistent with recently published studies[11–13]. Given that T_{FR} cells have been shown to mitigate germinal center responses in secondary lymphoid organs, it is tempting to assume that T_{FR} cells might not only impede anti-tumor immunity by inhibiting $CD8^+$ TILs, but also by regulating TLS in tumor tissues, which should be investigated in future studies.

Discussion

T_{REG} cells impede anti-tumor immunity and are thus detrimental to patient survival. In non-cancer settings, T_{REG} cells have been shown to differentiate into PD-1 expressing T_{FR} cells that restrain germinal center responses by suppressing GC B cells and stimulatory T_{FH} cells[2,41]**.** Both, T_{FH} and T_{FR} cells, constitutively express high levels of the co-inhibitory receptors PD-1, yet few studies have investigated their impact on anti-tumor immunity and their responsiveness to anti-PD-1 therapy. While recent studies have demonstrated that T_{FH} cells, B cells and TLS are associated with patient survival and responsiveness to immunotherapy[11–14], the precise mechanism, potential cell-cell interactions, drivers and regulators of TLS formation or maintenance, and the importance of specific B and T cell subsets remain unknown.

Here, we provide the first in-depth analysis of tumor-infiltrating T_{FR} cells and elucidate their responsiveness to ICB and the context in which they exert their suppressive functions. T_{FR} cells were prevalent in tumor tissues of several cancer types and

exhibited superior suppressive capacity and *in vivo* persistence when compared to T_{REG} cells, with whom they shared a clonal and developmental relationship. This developmental relationship between intratumoral T_{REG} and T_{FR} cells was characterized by substantial TCR sharing and a gradual increase of T_{FR} cells over time, which, together with the single cell trajectory analyses and adoptive transfer studies, implies ongoing T_{REG} to T_{FR} conversion. Crucially, unlike T_{REG} cells, T_{FR} cells were preferentially located within TLS, and among tumor-infiltrating lymphocytes, T_{FR} cells expressed the highest levels of CTLA-4 and PD-1. Given that T_{FR} cells mitigate germinal center responses in secondary lymphoid organs[2,41], our finding that T_{FR} cells are enriched in TLS suggests that intratumoral T_{FR} cells might also regulate TLS formation and maintenance, potentially by controlling B cell or T_{FH} cell responses, which should be tested in future studies.

Our findings in murine tumor models indicate that intratumoral T_{FR} cells are responsive to ICB and that by increasing the abundance of T_{FR} cells, anti-PD-1 therapy can not only facilitate, but also dampen anti-tumor immune attack. We provide critical insights into how anti-CTLA-4 and anti-PD-1 therapies mediate their function, and highlight the clinical benefit of sequential dosing to render tumors responsive to anti-PD1 therapy, a hypothesis that merits further investigation in a randomized clinical trial. The well-described clinical scenario in which some tumors hyper-progress following anti-PD1 therapy[42,43] may be explained by the effects of treatment on a highly suppressive immune cell compartment (T_{FR} cells), especially in patients with an initially high level of tumor-specific T_{REG} (T_{FR} precursor) cells. Conversely, exacerbated immune-related adverse events observed upon combination therapy, might be caused by anti-CTLA-4-mediated depletion or impairment of the activity of FOXP3-expressing cells in multiple tissues and subsequent uninhibited anti-PD-1-mediated activation of effector $CD4^+$ and $CD8^+$ T cells, hypotheses which can be addressed in future studies. Finally, our results implicate the unique composition of stimulatory *versus* suppressive T cells in the TME of each

patient, as well as their differentiation status (*i.e.*, PD-1 expression levels and frequency of T_{FR} cells within $CD4^+$ T cells), as important immunological determinants driving anti-PD-1 treatment efficacy.

References

1. De Simone, M. *et al.* Transcriptional Landscape of Human Tissue Lymphocytes Unveils Uniqueness of Tumor-Infiltrating T Regulatory Cells. *Immunity* **45**, 1135–1147 (2016).
2. Linterman, M. A. *et al.* Foxp3+ follicular regulatory T cells control the germinal center response. *Nat. Med.* **17**, 975–982 (2011).
3. Sage, P. T., Paterson, A. M., Lovitch, S. B. & Sharpe, A. H. The coinhibitory receptor CTLA-4 controls B cell responses by modulating T follicular helper, T follicular regulatory, and T regulatory cells. *Immunity* **41**, 1026–1039 (2014).
4. Sage, P. T., Alvarez, D., Godec, J., Von Andrian, U. H. & Sharpe, A. H. Circulating T follicular regulatory and helper cells have memory-like properties. *J. Clin. Invest.* **124**, 5191–5204 (2014).
5. Sage, P. T., Francisco, L. M., Carman, C. V. & Sharpe, A. H. The receptor PD-1 controls follicular regulatory T cells in the lymph nodes and blood. *Nat. Immunol.* **14**, 152–161 (2013).

6. Vanderleyden, I. *et al.* Follicular Regulatory T Cells Can Access the Germinal Center Independently of CXCR5. *Cell Rep.* **30**, 611-619.e4 (2020).

7. Brenna, E. *et al.* CD4+ T Follicular Helper Cells in Human Tonsils and Blood Are Clonally Convergent but Divergent from Non-Tfh CD4+ Cells. *Cell Rep.* **30**, 137-152.e5 (2020).

8. Romão, V. C. *et al.* Human blood T fr cells are indicators of ongoing humoral activity not fully licensed with suppressive function . *Sci. Immunol.* **2**, eaan1487 (2017).

9. Ritvo, P.-G. G. *et al.* T_{fr} cells lack IL-2Rα but express decoy IL-1R2 and IL-1Ra and suppress the IL-1–dependent activation of T_{fh} cells. *Sci. Immunol.* **2**, eaan0368 (2017).

10. Botta, D. *et al.* Dynamic regulation of T follicular regulatory cell responses by interleukin 2 during influenza infection. *Nat. Immunol.* **18**, 1249–1260 (2017).

11. Helmink, B. A. *et al.* B cells and tertiary lymphoid structures promote immunotherapy response. *Nature* **577**, 549-555 (2020)

12. Cabrita, R. *et al.* Tertiary lymphoid structures improve immunotherapy and survival in melanoma. *Nature* **577**, 561-565 (2020)

13. Petitprez, F. *et al.* B cells are associated with survival and immunotherapy response in sarcoma. *Nature* **577**, 556-560 (2020)

14. Hollern, D. P. *et al.* B Cells and T Follicular Helper Cells Mediate Response to Checkpoint Inhibitors in High Mutation Burden Mouse Models of Breast Cancer. *Cell*, **179**(5):1191-1206.e21 (2019)

15. Chung, Y. *et al.* Follicular regulatory T cells expressing Foxp3 and Bcl-6 suppress germinal center reactions. *Nat Med,* **18**(8):983-8.

16. Chen, X. *et al.* Cutting edge: expression of TNFR2 defines a maximally suppressive subset of mouse CD4+CD25+FoxP3+ T regulatory cells: applicability to tumor-infiltrating T regulatory cells. *J. Immunol.* **180**, 6467–6471 (2008).

17. Huang, C.-T. *et al.* Role of LAG-3 in regulatory T cells. *Immunity* **21**, 503–513 (2004).

18. Joller, N. *et al.* Treg cells expressing the coinhibitory molecule TIGIT selectively inhibit proinflammatory Th1 and Th17 cell responses. *Immunity* **40**, 569–581 (2014).

19. Hayatsu, N. *et al.* Analyses of a Mutant Foxp3 Allele Reveal BATF as a Critical Transcription Factor in the Differentiation and Accumulation of Tissue Regulatory T Cells. *Immunity* **47**, 268-283.e9 (2017).

20. Guo, X. *et al.* Global characterization of T cells in non-small-cell lung cancer by single-cell sequencing. *Nat Med*. **24**, 978-985 (2018).

21. Plitas, G. *et al.* Regulatory T Cells Exhibit Distinct Features in Human Breast Cancer. *Immunity* **45**, 1122–1134 (2016).

22. Miller, B. C. *et al.* Subsets of exhausted CD8 + T cells differentially mediate tumor control and respond to checkpoint blockade. *Nat. Immunol.* **20**, 326–336 (2019).

23. Im, S. J. *et al.* Defining CD8+ T cells that provide the proliferative burst after PD-1 therapy. *Nature* **537**, 417–421 (2016).

24. Utzschneider, D. T. *et al.* T Cell Factor 1-Expressing Memory-like CD8+ T Cells Sustain the Immune Response to Chronic Viral Infections. *Immunity* **45**, 415–427 (2016).

25. Siddiqui, I. *et al.* Intratumoral Tcf1+PD-1+CD8+ T Cells with Stem-like Properties Promote Tumor Control in Response to Vaccination and Checkpoint Blockade Immunotherapy. *Immunity* **50**, 1–17 (2019).

26. Sade-Feldman, M. *et al.* Defining T Cell States Associated with Response to Checkpoint Immunotherapy in Melanoma. *Cell* **175**, 998-1013.e20 (2018).

27. Ahmadzadeh, M. *et al.* Tumor-infiltrating human CD4+ regulatory T cells display a distinct TCR repertoire and exhibit tumor and neoantigen reactivity. *Sci. Immunol.* **4**, eaao4310 (2019).

28. Xu, L. *et al.* The Kinase mTORC1 Promotes the Generation and Suppressive Function of Follicular Regulatory T Cells. *Immunity* **47**, 538-551.e5 (2017).

29. Kniemeyer, O., Brakhage, A. A., Ferreira, F., Wallner, M. & Sawitzki, B. Regulatory T Cell Specificity Directs Tolerance versus Allergy against Aeroantigens in Humans. *Cell* **167**, 1067-1078.e16 (2016).

30. Szabo, P. A., Miron, M. & Farber, D. L. Location, location, location: Tissue resident memory T cells in mice and humans. *Sci. Immunol.* **4**, eaas9673 (2019).

31. Page, N. *et al.* Expression of the DNA-Binding Factor TOX Promotes the Encephalitogenic Potential of Microbe-Induced Autoreactive CD8+ T Cells. *Immunity* **48**, 937-950.e8 (2018).

32. Scott, A. C. *et al.* TOX is a critical regulator of tumour-specific T cell differentiation. *Nature* **571**, 270-274 (2019)

33. Tam, E. M. *et al.* Antibody-mediated targeting of TNFR2 activates CD8+ T cells in mice and promotes antitumor immunity. *Sci. Transl. Med.*, **11**(512):eaax0720 (2019)

34. Fu, W. *et al.* Deficiency in T follicular regulatory cells promotes autoimmunity. *J. Exp. Med.* **215**, 815–825 (2018).

35. Wu, H. *et al.* Follicular regulatory T cells repress cytokine production by follicular helper T cells and optimize IgG responses in mice. *Eur. J. Immunol.* **46**, 1152–1161 (2016).

36. Kleffel, S. *et al.* Melanoma Cell-Intrinsic PD-1 Receptor Functions Promote Tumor Growth. *Cell* **162**, 1242–1256 (2015).

37. Zhang, R. *et al.* An obligate cell-intrinsic function for CD28 in Tregs. *J. Clin. Invest.*, **123**(2):580-93 (2013)

38. Franckaert, D. *et al.* Promiscuous Foxp3-cre activity reveals a differential requirement for CD28 in Foxp3 + and Foxp3-T cells. *Immunol. Cell Biol.*, **93**(4):417-23 (2015)

39. Simpson, T. R. *et al.* Fc-dependent depletion of tumor-infiltrating regulatory T cells co-defines the efficacy of anti–CTLA-4 therapy against melanoma. *J. Exp. Med.* **210**, 1695–1710 (2013).

40. Wolchok, J. D. *et al.* Overall Survival with Combined Nivolumab and Ipilimumab in Advanced Melanoma. *N. Engl. J. Med.*, **377**(14):1345-1356 (2017).

41. Sage, P. T. *et al.* Suppression by T FR cells leads to durable and selective inhibition of B cell effector function. *Nat. Immunol.* **17**, 1436–1446 (2016).

42. Champiat, S. *et al.* Hyperprogressive disease is a new pattern of progression in cancer patients treated by anti-PD-1/PD-L1. *Clin. Cancer Res.* **23**, 1920–1928 (2017).

43. Knorr, D. A. & Ravetch, J. V. Immunotherapy and hyperprogression: Unwanted outcomes, unclear mechanism. *Clin. Cancer Res.* **25**, 904–906 (2019).

Acknowledgements

We thank L. Chudley, K. McCann, O. Wood, M. Chamberlain, K. Amer, D. Jeffrey, M. Lane, C. Fixmer, M. Lopez, N. Graham, M. Machado, T. Mellows and B. Johnson for assistance with recruitment of study subjects and processing of samples. We thank Dr. Matthew Wheater for the access to the clinical data from the joint practice with I.K and C.H.O. We thank A. Upadhye for contributions to experimental work. We thank J.B. Lilley for his help on the data collection and analysis of the survival cohort. We recognize C. Kim, D. Hinz and C. Dillingham for their assistance with cell sorting, FACSAria Fusion Cell Sorter - S10 RR027366; S. Liang, A. Wang and H. Simon for assistance with library preparation, next generation sequencing using Illumina HiSeq 2500 - NIH #S10OD016262 and NovaSeq6000 #S10OD025052-01. Members of the Vijayanand laboratory for their assistance with editing the figures and manuscript. We thank J. Linden and S.Fuchs for providing B16F10-OVA and MC38-OVA tumor cell lines, respectively. Supported by the Wessex Clinical Research Network and the National Institute of Health Research, UK (sample collection), the William K. Bowes Jr Foundation (P.V.), Whittaker foundation (T.S.-E. and C.H.O.), the Cancer Research UK Centres Network Accelerator Award Grant - A21998 (T.S.-E. and C.H.O.), the Faculty of Medicine of the University of Southampton (T.S.-E. and

C.H.O.) and Cancer Research UK (J.C., C.H.O.). The funders have no role in study design, data collection and analysis, decision to publish or preparation of the manuscript.

Author Contributions

S.E., J.C., P.S.F., T.S-E., F.A., C.H.O., and P.V., conceived of the work; S.E., J.C., performed experiments. S.E., J.C., B.P., C.R-S, and A.M., analyzed data under the supervision of F.A., C.H.O, P.V.; C.J.H., performed the immunohistochemistry analyses under supervision of G.J.T.; A.A., E.W., S.J.C., I.K., and S.E. assisted in patient recruitment, obtaining consent and sample collection; S.E wrote the first draft of the manuscript that was revised and edited by P.S.F., F.A., C.H.O., and P.V.

Declaration of Interests

The authors declare no competing interests.

Figure Legends

Figure 1. Tumor-infiltrating T_{FR} cells are highly prevalent in human cancers. a, Integrated analysis of 9 single-cell RNA-seq datasets displayed by uniform manifold approximation and projection (UMAP) from 6 different cancer types. Seurat clustering of 25,149 $CD4^+$ T cells colored based on cluster type (left panel) and study (middle panel); Right panel shows Seurat-normalized expression of *FOXP3* in different clusters (see also Fig. S1 and Methods). **b,c**, Bar charts depicting the frequency of $FOXP3^-$ and $FOXP3^+$ or T_{REG} in tumor-infiltrating $CD4^+$ T cells (**b**), or $BCL6^+$ T_{FR}, $CXCR5^+$ T_{FR}, $BCL6^+CXCR5^+$ T_{FR} in tumor-infiltrating T_{REG} cells (**c**) in the assessed datasets.

Figure 2. Tumor-infiltrating T_{FR} cells are primarily located in TLS. **a-d**, flow cytometric analysis and representative contour plots of $CD4^+$ T cells, T_{REG} cells, T_{FH} cells, T_{FR} cells, and histogram plots of $CD8^+$ and $CD4^+$ TILs from n=10 treatment naïve NSCLC patients depicting the frequency of $CD8^+$ T cells (blue, $LIN^-CD45^+CD3^+CD8^+$), T_{REG} (teal, $LIN^-CD45^+CD3^+CD4^+CXCR5^-CD127^-CD25^+$), T_{FH} (light green, $LIN^-CD45^+CD3^+CD4^+CXCR5^+GITR^-$) and T_{FR} (yellow, $LIN^-CD45^+CD3^+CD4^+CXCR5^+GITR^+$) cells (**a**), the frequency and mean fluorescence intensity (MFI) of CD25 and ICOS (%CD25, P=0,002; MFI CD25, P=0.0137; %ICOS, P=0.0645, MFI ICOS, P=0.0039 for indicated comparisons) (**b**) intracellular CTLA-4 expression and MFI in T_{REG} (teal, $LIN^-CD45^+CD3^+CD4^+CXCR5^-FOXP3^+BCL\text{-}6^-$), T_{FH} (light green, $LIN^-CD45^+CD3^+CD4^+BCL\text{-}6^+FOXP3^-$) and T_{FR} (yellow, $LIN^-CD45^+CD3^+CD4^+BCL\text{-}6^+FOXP3^+$) (%CTLA-4, P=0.0039, MFI CTLA-4, P=0.0020 for indicated comparisons) (**c**), and the frequency and MFI of PD-1 expression (%PD-1, P=0.0020; MFI PD-1, P=0.0020 for indicated comparisons) (**d**), grey depicts respective fluorescence minus one (FMO) controls in histogram plots. **e,** Whole-slide multiplexed immunohistochemistry analysis of T_{REG} and T_{FR} cells in NSCLC tissue sections from patients in **a-d**, Micrographs show PanCK (white), CD4 (light blue), CXCR5 (yellow), CD20 (magenta) FOXP3 (green) and BCL-6 (red), pink arrows characterize $CD4^+FOXP3^+BCL\text{-}6^+$ T_{FR} cells in a region of interest selected for high density of T_{FR} cells. Bar graphs show the proportion of $FOXP3^-$ and $FOXP3^+$ $CD4^+$ cells (upper panel) or T_{REG} and T_{FR} cells (lower panel) from whole-slide histo-cytometry analyses of each sample as in (**a-d**), scale bars are 250μm (left panel) and 25μm (right panel). **f**, Proportion of T_{REG} (teal) and T_{FR} (yellow) cells in tumor stroma versus tertiary lymphoid structures (TLS) (P=0.0002 (T_{REG}) and P=0.0002 (T_{FR}) from whole-slide histo-cytometry analyses for n=8 treatment naïve NSCLC patients. All data are mean +/- S.E.M.; Two-tailed Wilcoxon matched-pairs signed rank test between T_{REG} and T_{FR} cells (**b-d**) and two-tailed Mann-Whitney test between TLS and stroma localization for T_{REG} and T_{FR} cells (**f**).

Figure 3. Comparison of human tumor-infiltrating T_{REG} and T_{FR} cells. a, Analysis of 10x single-cell RNA-seq data displayed by manifold approximation and projection (UMAP). Seurat clustering of 8,722 $CD4^+$ and $CD8^+$ T cells from primary tumor tissue and metastasized tumor-infiltrated lymph nodes colored based on cluster type (left panel), the other three panels are showing Seurat-normalized expression of *CD8B*, *CD4* and *FOXP3* respectively. **b**, Heatmap comparing gene expression of cells in cluster 1 versus cluster 6. Depicted are transcripts that change in expression more than 0.25-fold and adjusted *P* value of ≤ 0.05. **c,d** Gene set enrichment analysis for follicular feature[44] (**c**) and T_{FR} feature genes (**d)**, derived from **Fig. 3j**) for cells in cluster 6 and cluster 1 ordered by Log2 fold change. **e**, Ingenuity pathway analysis of differentially expressed transcripts (n=1245) between cluster 1 and cluster 6. **f**, Violin plots comparing expression levels of indicated transcripts in cluster 1 (left) and cluster 6 (right) cells. **g**, TraCer plots of all clonally expanded cells (=/>2 clonotypes) in cluster 1 and cluster 6 colored by cluster origin (cluster 1 green, cluster 6 yellow). **h**, Euler diagram shows overlap between clonotypes in cluster 1 and cluster 6. **i**, bar chart depicting the mean percentage of clonally expanded cells in cluster 1 and cluster 6. **j**, Heatmap illustrating the intersection of differentially expressed genes (with mean TPM >25) when comparing *4-1BB*$^-$ T_{REG} cells with three populations: *4-1BB*$^+$ T_{REG}, clonally-expanded T_{REG} cells sharing their TCRs with T_{FR} and clonally-expanded T_{FR} cells (distinct cell populations are indicated with colored bars). Genes linked to immunosuppressive function, co-stimulation, and tissue residency are highlighted.

Figure 4. Frequency and functional responsiveness of T_{FR} cells in murine tumor models. a-c, Mice were inoculated with B16F10-OVA or MC38-OVA cells subcutaneously (*s.c.*) on the right flank. Analyses of tumor-infiltrating T_{REG} ($CD19^-$

498 $CD45^+CD3^+CD4^+BCL\text{-}6^-FOXP3^+$) and T_{FR} ($CD19^-CD45^+CD3^+CD4^+BCL\text{-}6^+FOXP3^+$) cells were performed, **a**, Flow-cytometric analysis
499 of the frequency of tumor-infiltrating T_{REG} and T_{FR} cells in indicated tumor models at day 21 after tumor inoculation (n=6 mice for
500 B16F10 and n=7 mice for MC38). **b**, Flow-cytometric analysis of the MFI and frequencies of expression of KI-67 (P=0.002), TCF-1
501 (P=0.002) and 4-1BB (0.002) in indicated cell types in the B16F10-OVA model at day14 after tumor inoculation (n=10 mice/group). **c**,
502 Representative FACS plots depicting the expression of TOX (x-axis) and TCF-1 (y-axis) in $CD8^+$ T cells, T_{REG} cells and T_{FR} cells,
503 Flow-cytometric analysis of the frequency of TOX-expressing cells in indicated cell types in the B16F10-OVA model at day14 (n=10
504 mice/group). **d**, Mice were immunized intraperitoneally (*i.p.*) with Ovalbumin in alum and treated with an IL-2/anti-IL2R complex at
505 days 3,4 and 5 for *in vivo* T_{REG} cell expansion; shown are representative FACS plots characterizing splenic T_{REG} ($CD4^+CXCR5^-$
506 $CD25^+GITR^+$) and T_{FR} ($CD4^+CXCR5^+CD25^+GITR^+$) cells, **e**, Representative histogram plots depicting the dilution of cell trace violet
507 (CTV) in $CD8^+$T cells with or without addition of T_{REG} or T_{FR} cells. **f**, Flow-cytometric analysis of an *in vitro* proliferation assay showing
508 the frequency of proliferating $CD8^+$ T cells when co-cultured with different proportions of T_{REG} cells (green) or T_{FR} cells (yellow),
509 depicted are the results for n=3 technical replicates for the dilutions and n=4 technical replicates for $CD8^+$ T cells (1:0 dilution). **g**,
510 Luminex analysis of supernatants from an *in vitro* proliferation assay (**e,f**), depicted is the concentration of secreted IFN-γ, IL-2 and
511 TNF for n=2 technical replicates. **h**, fold-change reduction in secretion of indicated cytokines between T_{REG} and T_{FR} cells at a 4:1 ratio
512 of CD8 T cells to either T_{REG} or T_{FR} cells. **i**, indicated cells were transferred into B16F10-OVA tumor-bearing $RAG1^{-/-}$ recipient mice at
513 day 3 after tumor inoculation, tumor volume of mice treated as indicated is shown (n=5 mice/group). Data are mean +/- S.E.M.;
514 Significance for comparisons were computed using two-tailed Mann-Whitney test. All data are representative of two independent
515 experiments.

Figure 5. Intratumoral T_{FR} cells gradually increase over time. a, Analysis of 10x single-cell RNA-seq data displayed by uniform manifold approximation and projection (UMAP). Seurat clustering of tumor-infiltrating FOXP3-expressing T cells colored based on cluster type, the panels shows UMAPs of tumor-infiltrating FOXP3-expressing T cells at d11 (left panel) and d18 (right panel). Charts show proportion of cells in individual mice for the indicated time point. Percentages for cells in cluster 2 (T_{FR} cells) are depicted. **b**, Heatmap showing genes enriched in the identified clusters. Depicted are transcripts that significant change in expression (> 2-fold and adjusted *P* value of ≤ 0.05.) **c**, Bar charts depicting the proportion of cells in each cluster, colored based on tumor developmental stage (d11 *versus* d18). **d,e,** Gene set enrichment analysis for a T cell activation signature (**d**), T_{FH} signatures[44] (**e**), derived from **Extended Data Fig. 2a-e**, and T_{FR} signature genes (**e)**, derived from **Fig. 2j** and **Extended Data Fig. 2a-e**) for cells in cluster 2 *versus* the other clusters ordered by Log2 fold change. **f**, Volcano plot of cells in cluster 2 *versus* the other clusters, depicted are differentially expressed transcripts (adjusted *P* value of ≤ 0.05) that change in expression more than 2-fold. **g**, Plot shows average transcript expression (color scale) and percent of expressing cells (size scale) for selected genes in each cluster. **h**, Euler diagram shows overlap between clonotypes in cluster 2 and the other clusters. **i**, Single-cell pseudo-time trajectory analysis of tumor-infiltrating FOXP3-expressing T cells (**a**) constructed using the Monocle3 algorithm. **j**, Flow-cytometric analysis depicting the MFI of the expression of PD-1 (P=0.002) and CTLA-4 (P=0.002) in indicated cell types in the B16F10-OVA model at day14 after tumor inoculation. Representative histogram plots are displayed. Data in (**j**) are mean +/- S.E.M.; Significance for comparisons were computed using two-tailed Wilcoxon matched-pairs signed rank test. Data in (**j**) are representative of two independent experiments.

Figure 6. T_{FR} cells are highly responsive to ICB. a, Mice were *s.c.* inoculated with B16F10-OVA or MC38-OVA cells and treated with anti-PD-1 Abs at indicated time points. Flow-cytometric analysis of the frequency of tumor-infiltrating T_{REG} and T_{FR} cells, as well

as fold induction of both cell types following anti-PD-1 therapy in the B16F10-OVA model (left panel, n=9 mice/group) and MC38-OVA model (right panel, n=5 mice/group). **b**,**c** *Foxp3*$^{YFPcre/YFPcre}$ *Bcl6*$^{fl/fl}$ (T_{FR} knockout) mice or *Foxp3*$^{YFPcre/YFPcre}$ *Bcl6*$^{+/+}$ control mice were *s.c.* inoculated with B16F10-OVA cells and treated with isotype control or anti-PD-1 Abs at indicated time points, Tumor volume (**b**) for n=7-9 mice/group and frequency of granzyme B^{+}CD8^{+} T cells in tumor-draining lymph nodes (**c**) of mice treated as indicated in (**b**), n=7-9 mice/group. **d**, Mice were immunized i.p. with Ovalbumin in alum and additionally treated with an IL-2/anti-IL-2R complex at days 3,4 and 5. OT-I CD8^{+} T cells, GFP^{+} and YFP^{+} T_{REG} cells were adoptively transferred into B16F10-OVA tumor-bearing RAG1$^{-/-}$ mice at day 3 after tumor inoculation. In n=7 mice, the frequencies of eGFP and YFP cells in spleen (left, P=0.007) or tumor tissue (right, P=0.0006) are shown. **e**, Flow-cytometric analysis of BCL-6 expression in splenic CD4^{+}FOXP3^{+} cells of *Foxp3*$^{YFP\text{-}cre}$ x *Bcl6*$^{fl/fl}$ mice (grey), *Foxp3*^{eGFP} mice (blue) and tumor-infiltrating CD4^{+}FOXP3^{+} cells (red) 13 days after adoptive transfer into B16F10-OVA tumor-bearing RAG1 KO mice. **f,** Mice were immunized i.p. with Ovalbumin in alum and additionally treated with an IL-2/anti-IL-2R complex at days 3,4 and 5. OT-I CD8^{+} T cells, RFP^{+} and YFP^{+} T_{REG} cells were adoptively transferred into B16F10-OVA tumor-bearing Rag1 KO mice at day 3 after tumor inoculation. In n=6 mice/group, the frequencies of RFP^{+} and YFP^{+} in spleen (left, P=0.0087) or tumor tissue (right, P=0.0022) are shown. Data are mean +/- S.E.M.; Significance for comparisons were computed using two-tailed Mann-Whitney test (**a,b,d,f**) or one-way ANOVA comparing the mean of each group with the mean of the control group (ctrl+anti-PD-1) followed by Dunnett's test (**c**). All data are representative of two independent experiments.

Figure 7. Clinical benefit of sequential ICB. a-c, Mice were *s.c.* inoculated with B16F10-OVA cells and treated with anti-CTLA-4 (day 10 and day 13, n=8 mice), anti-PD-1 (day 14 and day 17, n=10 mice), anti-CTLA-4 (day 10 and day 13) and anti-PD-1 Abs (day 14 and day17) (n=8 mice) or isotype treated control mice (n= 13 mice) at indicated time points, tumor volume (**a**) and cell frequencies

(**b**) of mice treated as indicated. (P-value style for **a,b=** 0.1234 (ns), 0.0332 (*), 0.0021 (**), 0.0002 (***), <0.0001 (****)) **c**, Survival curves of an independent cohort of melanoma patients (n=271) stratified into 5 groups based on ICB treatment regimen. **d,e**, Survival curves for patients stratified into those with early onset disease (**d**) (M1a and M1b combined), late stage disease (**e**) (M1c and M1d combined) or BRAF mutation status (**f**) of patient cohort. Two-tailed Mann-Whitney test (**a**), one-way ANOVA was used to compare the mean of each group with the mean of the control group (B16F10) followed by Dunnett's test (**b**) or Mantel-Cox test (**c-e**). Data in **a,b** are mean +/- S.E.M and are representative of two independent experiments.

Methods

Human tumor samples. The study was approved by the Southampton and South West Hampshire Research Ethics Board (ethics committee MREC number 14/SC/0186, NIHR portfolio adoption ID 16818), and written informed consent was obtained from all subjects. Newly diagnosed, untreated patients with NSCLC (or HNSCC), were prospectively recruited once referred. Freshly resected tumor tissue was obtained from lung cancer patients following surgical resection and after histological confirmation. The patient cohort for the survival analysis was collected by retrospective evaluation of a centralized prescribing system (Aria, Varian Medical Systems Inc). All patients started on immunotherapy at a single institution (Southampton University Hospitals NHS Foundation Trust) with immunotherapy for melanoma between 07/2014 to 10/2018 were included. Patients were divided into cohorts according to first type immunotherapy treatment approved in the United Kingdom (anti-PD-1, either nivolumab or pembrolizumab, N=98), anti-CTLA-4 antibody (ipilimumab (88) or joint administration of nivolumab plus ipilimumab on up to four occasions (N=85), followed by maintenance nivolumab where appropriate. Dosing was according to standard of care at the time (3mg/kg ipilimumab x 4, 2mg/kg of pembrolizumab 3 weekly, later 200mg flat dosing, 3mg/kg nivolumab, then 480mg flat dosing, and in combination

3mg/kg ipilimumab + 1mg/kg nivolumab, four doses, followed by 3mg/kg nivolumab). All patients were included who had at least one dose of immunotherapy. Clinical data were obtained from an electronic hospital record for age, gender, BRAF status, LDH, M stage, performance status. For clinical outcome overall survival was collected to death or censored at last clinical review. Data were anonymized by the treating clinician (I.K. and C.H.O.) once the data had been collated and verified. Prism 8 (Graph Pad Software) was used for ANOVA and to plot Kaplan Meier Survival Graphs and estimate treatment differences using a Log-rank (Mantel-Cox) test on survival curves. SPSS v26 (IBM Corp) was used to evaluate imbalances between treatment groups via Chi Square testing followed by Cox Regression analysis. Fur multiple testing a Bonferroni error correction was applied.

Mice. C57BL/6J (JAX stock #000664), *Bcl6*$^{fl/fl}$ (JAX stock #023727), OT-I (JAX stock #003831) and RAG1 KO (JAX stock #002216), *Foxp3*$^{YFP\text{-}cre}$ (JAX stock #016959) mice were obtained from Jackson labs. *Foxp3*$^{eGFP\text{-}cre\text{-}ERT2}$ (JAX stock #016961) and *Foxp3*^{RFP} (JAX stock #008374) were a kind gift from K. Ley (LJI) and *Foxp3*^{eGFP} (JAX stok #006772) mice were a kind gift from A. Altman (LJI). Female mice (age 6-12 weeks) were used for all experiments. The housing temperature in the vivarium is controlled and ranges from 69-75F, humidity is not controlled but monitored and ranges from 30-70%. The light/dark cycles are from 6am-6pm, respectively. All animal work was approved by the relevant La Jolla institute for Immunology Animal Ethics Committee.

Tumor cell lines. B16F10-OVA cells were a gift from the laboratory of J. Linden (LJI) and MC38-OVA cells were a gift from the lab S. Fuchs (UPenn) and approved for use by M. Smyth (Peter MacCallum cancer center). Cell lines tested negative for mycoplasma infection and were subsequently treated with Plasmocin to prevent contamination.

Tumor models. Tumor cell lines were tested negatively for mycoplasma infection and Plasmocin (InvivoGen) was used as a routine addition to culture media to prevent mycoplasma contamination. Mice were inoculated with 1-1.5x10^5 B16F10-OVA cells or 2x10^6

MC38-OVA cells subcutaneously into the right flank. Mice were injected intraperitoneally at indicated time points with either 200µg anti-PD-1 (29F1.A12, *InvivoPlus* anti-mouse PD-1, Bioxcell), anti-CTLA-4 (9H10, *InvivoPlus* anti-mouse CTLA-4, Bioxcell) or respective isotype controls (anti-CTLA-4 isotype ctrl, *InVivo*Plus polyclonal Syrian hamster IgG, Bioxcell) (anti-PD-1 isotype control, *InVivo*Plus rat IgG2a isotype control, anti-trinitrophenol, Bioxcell). Tumor size was monitored every other day, and tumor harvested at indicated time points for analysis of tumor-infiltrating lymphocytes. Tumor volume was calculated as ½ x D x d^2, where D is the major axis and d is the minor axis, as described previously[45]. Tumor growth was monitored at least thrice weekly to ensure that tumors did not exceed 25mm in diameter.

Suppression and Competition Assay. Mice were immunized i.p. with Ovalbumin in alum (100µg in 100µl sterile PBS mixed with 100µl 2%alum). At day 3-5 after immunization, mice were immunized i.p. with an IL-2/anti-IL-2Receptor complex (1µg IL-2, 5µg anti-IL-2Receptor Ab, mixed for 30min at 37 °C) to achieve polyclonal expansion of T_{REG} cells in vivo, as described previously[46]. Lymphocytes ($CD4^+$ and $CD8^+$ T cells) were isolated from spleen by mechanical dispersion through a 70-µm cell strainer (Miltenyi) to generate single-cell suspensions. $CD4^+$ and $CD8^+$ T cells were purified (Stemcell) according to manufacturer's instructions.

In Vitro – $CD8^+$ T cells were labelled with CellTrace Violet (CTV) (Thermofisher) and 40,000 cells were added to 96 well cell culture plated, pre-coated with anti-CD3, in 200µl complete RPMI media. Purified $CD4^+$ T cells were stained and different numbers of viable (Fixable Viability dye) T_{REG} cells ($CD4^+CXCR5^-CD25^+GITR^+$) or T_{FR} cells ($CD4^+CXCR5^+CD25^+GITR^+$) were sorted into the cell culture plate containing the CTV-labeled $CD8^+$ T cells. $CD8^+$ T cell proliferation (CTV dilution) was determined 3 days later.

In Vivo – OT-I $CD8^+$ T cells were purified (Stemcell), $CD4^+$ T cells were purified, stained and T_{REG} and T_{FR} cells were sorted as described above. Cells were counted and $2x10^5$ OT-I T cells, $2x10^5$ OT-I T cells + $5x10^4$ T_{REG} cells (4:1 ratio) or $2x10^5$ OT-I T cells +

611 $5x10^4$ T_{FR} cells (4:1 ratio) were adoptively transferred into B16F10-OVA tumor-bearing RAG1 KO recipient mice 3 days after tumor
612 inoculation.
613 Competition assay – OT-I $CD8^+$ T cells were purified (Stemcell), $FOXP3^+$ T cells were purified from *Foxp3*$^{YFP\text{-}cre}$ x *Bcl6*$^{fl/fl}$ mice (YFP^+)
614 and *Foxp3*^{eGFP} mice (GFP^+) or from Foxp3^{RFP} mice for the control experiments and $4x10^5$ cells ($2x10^5$ OT-I T cells, $1x10^5$ GFP^+ or
615 RFP^+ T_{REG} cells and $1x10^5$ YFP^+ T_{REG} cells) were adoptively transferred into B16F10-OVA tumor-bearing RAG1 KO recipient mice 3
616 days after tumor inoculation.
617
618 **Flow cytometry.** T cells from cryopreserved tumor tissue was mechanically dissociated and digested enzymatically as previously
619 described[47]. Cells were treated with FcR blocking antibody (BD Biosciences) and stained in PBS with 2%FBS, 2mM EDTA for 30
620 minutes at 4°C. For selected markers, secondary stains were performed. Samples were subsequently sorted or fixed for intracellular
621 staining with the FOXP3 TF kit (eBioscience) according to manufacturer's instructions. For all staining, cell viability was verified using
622 fixable viability dye (ThermoFisher).
623 Murine samples – Lymphocytes were isolated from spleen by mechanical dispersion through a 70-µm cell strainer (Miltenyi) to
624 generate single-cell suspensions. RBC lysis (Biolegend) was performed to remove red blood cells. Tumor samples were harvested
625 and lymphocytes were isolated by dispersing the tumor tissue in 2ml of PBS, followed by incubation of samples at 37°C for 15min
626 with DNase I (Sigma) and Liberase DL (Roche). Samples were passed through a 70-µm cell strainer to create single-cell
627 suspensions. Cells were prepared in staining buffer (PBS with 2% FBS and 2mM EDTA) and FcR blocked (clone 2.4G2, BD
628 Biosciences) and stained with indicated primary antibodies for 30 minutes at 4°C; secondary stains were done for selected markers.
629 Samples were then sorted or fixed and intracellularly stained using a FOXP3 transcription factor kit according to manufacturer's

instructions (eBioscience). Cell viability was determined using fixable viability dye (ThermoFisher). For bulk-RNA-seq analyses, we sorted tumor-infiltrating T_{FR} cells based on the co-expression of CXCR5 and GITR[2,5] (**Extended Data Fig. 1b**), a surface marker that distinguishes T_{FH} cells from T_{FR} cells. To accurately assess the expression of intracellularly stored molecules like CTLA-4, we characterized T_{FR} cells based on co-expression of BCL-6 and FOXP3 (**Extended Data Fig. 1c**) since cell fixation led to epitope masking of CXCR5 (**Extended Data Fig. 1c**, bottom left plot) and GITR. All samples were acquired on a BD FACS Fortessa or sorted on a BD FACS Fusion (both BD Biosciences) and analyzed using FlowJo 10.4.1.

Histology and immunohistochemistry.

The primary antibodies used for IHC include anti-CD8 (pre-diluted, C8/144B, Agilent Dako), anti-CD4 (1:100, 4B12, Agilent Dako), anti-FOXP3 (1:100, ab20034, Abcam), anti-CXCR5 (1:50, D6L3C, CellSignaling), anti-BCL-6 (1:30, NCL-L-Bcl6-6-564, Leica), anti-CD31 (pre-diluted product diluted further 1:5, Agilent Dako) and anti-PanCK (AE1/AE3; pre-diluted; Agilent Dako). Samples for immunohistochemistry analyses were prepared, stained and analyzed as previously described[48]. Cells were identified by nucleus detection and cytoplasmic regions were simulated up to 5µm, per cell protein expression was measured using the mean staining intensity within simulated cell regions.

Bulk-RNA sequencing. Total RNA was purified using a miRNAeasy kit (Qiagen) from human tumor-infiltrating T_{REG} (LIN^- $CD45^+CD3^+CD4^+CXCR5^-CD127^-CD25^+$) and T_{FR} ($LIN^-CD45^+CD3^+CD4^+CXCR5^+GITR^+$) cells and was quantified as described previously[47,49]. Cells from mice immunized with either Ovalbumin in Complete Freund's adjuvant (InvivoGen), Ovalbumin in Monophosphoryl Lipid A (InvivoGen) or mock PBS: T_{EFF} ($CD19^-CD45^+CD3^+CD4^+CXCR5^-GITR^-CD25^-CD62L^-CD44^+$), T_{REG} ($CD19^-$ $CD45^+CD3^+CD4^+CXCR5^-GITR^+CD25^+$), T_{FH} ($CD19^-CD45^+CD3^+CD4^+CXCR5^+GITR^-$) and T_{FR} ($CD19^-$

650 $CD45^+CD3^+CD4^+CXCR5^+GITR^+$) were sorted and RNA was purified as described above. RNA-seq libraries were prepared using
651 Smart-seq2 protocol and sequenced on Illumina platform, as previously described[50]. Quality control steps were applied as previously
652 described[47]. Samples failing quality controls, or having a low number of cells were excluded from further sequencing and analysis.
653
654 **Bulk RNA-seq analysis.** Bulk RNA-seq data from human samples were mapped against the hg19 reference using TopHat[51] (--
655 bowtie1 –max-multihits 1 –microexon search) with FastQC (v0.11.2), Bowtie[52] (v1.1.2), Samtools (v0.1.19.0)[53] and we employed
656 htseq-count -m union -s no -t exon -i gene_name (part of the HTSeq framework, version v0.7.1)[54]. Trimmomatic (v0.36) was used to
657 remove adapters[55]. Bulk RNA-seq from mouse samples were mapped against mm10 reference using TopHat (1.4.1) with library-type
658 fr-unstranded parameter. Values throughout are displayed as $\log_2$ TPM (transcripts per million) counts; a value of 1 was added prior
659 to log transformation. To identify genes expressed differentially by various cell types, we performed negative binomial tests for
660 unpaired comparisons by employing the Bioconductor package DESeq2[56] (v1.14.1), disabling the default options for independent
661 filtering and Cooks cutoff. We considered genes to be expressed differentially by any comparison when the DESeq2 analysis
662 resulted in a Benjamini-Hochberg–adjusted *P* value of ≤ 0.05 and a fold change of at least 2. Euler diagrams were generated using
663 the eulerr package (v5.1.0). Correlations and heatmaps were generated as previously described[49,57,58]. Visualizations were generated
664 in ggplot2 using custom scripts. For tSNE analysis, the data frame was filtered to genes with mean ≥ 1 TPM counts expression in at
665 least one condition and visualizations created using the top 500 most variable genes, as calculated in DESeq2[56] (v1.16.1); this
666 allowed for unbiased visualization of the Log_2 (TPM counts + 1) data, using package Rtsne (v0.13). Data in heatmaps are shown as
667 log2 normalized z-scores.
668

669 **Weighted Gene Coexpression Network Analysis.** WGCNA was completed in R (v.3.5.0) with the package WGCNA *(v1.61)* using
670 the TPM data matrix. Well-expressed genes with TPM >= 10 in at least one sample, were used in both T_{FR} and T_{REG} data from
671 human. Gene modules were generated using blockwiseModules function (parameters: checkMissingData = TRUE, power = 5,
672 TOMType = "signed", minModuleSize = 30, maxBlockSize = 13441, mergeCutHeight = 0.80). The remaining parameters were as per
673 default in WGCNA. The default 'grey' module generated by WGCNA for non-co-expressed genes, was excluded from further
674 analysis. As each module by definition is comprised of highly correlated genes, their combined expression may be usefully
675 summarized by module eigengene (ME) profiles, effectively the first principal component of a given module. A small number of
676 module eigengene profiles may effectively 'summarize' the principle patterns within the transcriptome with minimal loss of
677 information. This dimensionality-reduction approach aids correlation of MEs with clinical traits as a module-trait relationship matrix.
678 Significance of correlation between this trait and MEs was assessed using linear regression with Benjamini-Hochberg adjustment to
679 correct for multiple testing. The TOMplot was generated using the TOMplot function in WGCNA with default parameters for clustering
680 and color scheme. To visualize co-expression networks were generated in gplots (v3.0.1) using the heatmap2 function, while
681 weighted correlation analysis was completed using WGCNA [59] (v1.61*)* from the Log_2 (TPM counts + 1) data matrix and the function
682 *TOMsimilarityfromExpr* (Beta = 5) and *exportNetworkToCytoscape*, weighted = true, threshold = 0.05. Highlighted genes were
683 ordered as per the order in the correlation plot. Networks were generated in Gephi (v0.92) [60,61] using ForceAtlas2 and Noverlap
684 functions. Color and size were scaled to the *Average Degree* calculated in Gephi. Edge width was scaled to the WGCNA edge
685 weight value.
686

Meta-analysis of published single-cell RNA-seq studies. We integrated 9 published single-cell RNA-seq datasets[20,26,62–68] of tumor-infiltrating *CD4*-expressing T cells with UMAP. The integration was performed using the R package Seurat v3.0. For each dataset, cells that expressed less than 200 genes were considered outliers and discarded. We integrated data from all cohorts using the alignment by 'anchors' option in Seurat 3.0. Briefly, the alignment is a computational strategy to "anchor" diverse datasets together, facilitating the integration and comparison of single cell measurements from different technologies and modalities. The "anchors" correspond to similar biological states between datasets. These pairwise correspondences between datasets allows the transformation of datasets into a shared space regardless of the existence of large technical and/or biological divergences. This improved function in Seurat 3.0 allows integration of multiple RNA-seq datasets generated by different platforms[69]. While we agree that single cell RNA-seq can be utilized to identify distinct states within a given cell population, it does not offer higher resolution compared to bulk RNA-seq in terms of number of transcripts recovered due to high drop-out rates with single-cell RNA-seq assays, more so with 10X-based assays. We used the FindIntegrationAnchors function to find correspondences across the different study datasets with default parameters (dimensionality = 1:30). Furthermore, we used the IntegrateData function to generate a Seurat Object with an integrated and batch-corrected expression matrix. In total, 25,149 cells and 2,000 most variable genes were used for clustering. We used the standard workflow from Seurat, scaling the integrated data, finding relevant components with PCA and visualizing the results with UMAP. The number of relevant components was determined from an elbow plot. UMAP dimensionality reduction and clustering were applied with the following parameters: 2000 genes, 15 principal components, resolution of 0.2, min.dis 0.05 and spread 2. Cells used for the integration were selected from clusters labeled in the original studies as tumor CD4 T cells and from pre-treatment samples when necessary. Cells with expression of *CD8B* > 1 CPM (UMI data) or 10 TPM (Smart-seq2) were

filtered out as indicated in Table 1. T_{REG} cells and T_{FR} cells were identified based on criteria defined in Table 1. Only Smart-seq2 datasets were used to compare T_{FR} cells from different cancer types.

Single-cell differential expression analysis. Differential expression was calculated with MAST[70] and SCDE[71] (v1.99.1) as previously described[57]. For each comparison, we obtained the differentially expressed gene lists by taking the union of the gene lists from both the methods using adjusted $P < 0.05$ and $\log_2$ fold change > 1 from each method.

Single-cell TCR and transcriptome analysis: Single-cell Smart-seq2 data from[20] were re-analyzed (**Table 1**), using custom scripts to identify αβ chains and showing only cells were both TCR chains were detected, as described previously[56]. Visualizations were completed in ggplot2, Prism (v8.1.1) and custom scripts in TraCer. A cell was considered expanded when both the most highly expressed α and β TCR chain sequences matched other cells with the same stringent criteria. Cells were considered not expanded when α and β TCR productive chain sequences did not match those of any other cells. A cell was considered a T_{REG} cell when the expression of *CD4* and *FOXP3* were > 10 TPM, and lacked expression of *CXCR5* and *BCL6* (TPM ≤10). A cell was characterized as a T_{FR} cell if expression of *CD4* and *FOXP3* were > 10 TPM and the expression of *CXCR5* or *BCL6* was > 10 TPM. A cell was considered *4-1BB*$^+$ when the expression of *4-1BB* was > 10 TPM as indicated in Table 1. Cell-state hierarchy maps were generated using Monocle (v3.0)[72] and default settings with expressionFamily = negbinomial.size(), lowerDetectionLimit = 0.1 after transformation of TPM counts with relative2abs function as recommended in the manual, including the top 2000 most variable genes identified in Seurat (v3.0) and taking 14 PCs based on the elbow plot. The shared signature was calculated with AddModuleScore function from Seurat after setting the object with default parameters and using the intersection of differentially expressed genes from comparing *4-1BB*$^-$ T_{REG} cells with with three populations: *4-1BB*$^+$ T_{REG}, clonally-expanded T_{REG} cells sharing their TCRs with T_{FR} and

clonally-expanded T_{FR} cells with Benjamini-Hochberg–adjusted P value of < 0.05 and a log2 fold change of 1.Single-cell smart-seq2 data from[26] were utilized to compare the single-cell transcriptome of tumor-infiltrating T_{FR} cells from pre- and post-anti-PD-1 treatment samples. Data in heatmaps are shown as log2 normalized z-scores.

Hierarchical clustering. Distance between clusters was calculated by obtaining a particular cells location in PCA space (Principal component 1:5) using the function Embeddings from Seurat. The number of principal components was determined from an elbow plot. A distance matrix was calculated (*dist function*, core R, method = Euclidean) from the PCA matrix and the clustering was performed (*hclust* function, method="average") in R and generated from the distance matrix. Function colored_bars from the WGCNA package was used to annotate different groups in the dendrogram.

Single-cell transcriptome analysis of primary tumor tissue and metastatic tumor-infiltrated lymph nodes. Human T cells from 2 HNSCC patients (primary tumor tissue and metastatic tumor-infiltrated lymph nodes) were isolated and prepared as described above. $CD4^+$ T_H cells ($CXCR5^+GITR^-$ and $CXCR5^-CD25^-$), T_{REG} cells ($CD4^+CXCR5^-CD25^+CD127^{lo}$), T_{FR} cells ($CD4^+CXCR5^+GITR^+$) and $CD8^+CD69^+$ cells were sorted and cDNA libraries were constructed using the standard 10x sequencing protocol. A total of n=9,562 (n=4,975 from metastatic tumor-infiltrated lymph node, n=4,589 from primary tumor tissue) cells were sequenced and cells with less than 200 and more than 5,000 expressed genes, less than 15,000 counts, and more than 10 % of mitochondrial counts were filtered out. For clustering with Seurat (3.0) we used 17 PCs from a set of highly variable genes (n = 609) taking 30 % of the variance after filtering out genes with mean expression less than 0.1 and removing TCR genes. TCR analysis: clonotype output (clonotypes and filtered contig annotation) from Cell Ranger for tumor and lymph node libraries were re-calculated (matching sequences were assigned the same clonotype id) and the overlap between cluster 1 and 6 was determined with these 'aggregated'

tables. Gene Set Enrichment analysis: the Log2 fold change was used as ranking metric and enrichment was calculated for each list. The package fgsea (v1.13.0) in R with default parameters was used to calculate the enrichment and create GSEA plots. Monocle (v2.99.1) was used to generate the trajectory plots, reduction_method = DDRTree for the dimensional reduction taking 15 principal components. Hierarchical clustering was performed as stated above using 20 PCs.

Single-cell transcriptome analysis of tumor-infiltrating FOXP3-expressing cells. FOXP3-expressing (RFP^+) cells were isolated from tumor tissues at day 11 or day 18 after B16F10-OVA tumor-inoculation of *Foxp3*^{RFP} reporter mice. Four mice from each time point were barcoded with murine Totalseq-C antibodies (Biolegend). Live/$Dead^-CD19^-CD3^+CD4^+RFP^+$ cells were sorted and cDNA libraries were constructed using the standard 10x sequencing protocol. Gene expression, TCR, and antibody capture data was processed with Cell Ranger (v3.1.0). Antibody capture data was analyzed with custom scripts (github.com/vijaybioinfo/ab_capture) as previously described[73]. Differential gene expression analysis was performed as described above. One contaminating cluster exhibiting high expression of transcripts associated with non-T_{REG} cells (i.e. *CD40Lg*) was removed prior to differential gene expression analysis. Finally, TCR data was analyzed using custom scripts in R taking clone data for each barcode as indicated in Cell Ranger's output. Euler diagrams and Enrichment plots were generated with eulerr (v6.1.0) and fgsea (v1.10.1), respectively.

Accession codes

Expression data has been deposited in the Gene Expression Omnibus database under the Super Series Accession Number GSE132297. This Super Series includes data from human and mouse samples.

Code availability

Scripts used for this study are available in our repository on GitHub (https://github.com/vijaybioinfo/TFR_2021). An explanation of each of the is included as well as version changes.

Quantification and statistical analysis

The number of subjects, samples or mice/group, replication in independent experiments, and statistical tests can be found in the figure legends. Details on quality control, sample elimination and displayed data are stated in the method details and figure legends. Sample sizes were chosen based on published studies to ensure sufficient numbers of mice in each group enabling reliable statistical testing and accounting for variability. Sample sizes are indicated in Figure legends. Mice, which didn't develop any tumors by 10 after inoculation were excluded from analyses, prior to any therapeutic intervention. RNA-seq samples that didn't pass quality control weren't included in the analyses. Experiments were reliably reproduced in independent experiments at least twice. Only female mice were used in the experiments and animals of similar age were randomly assigned to experimental groups. Statistical analyses were performed with Graph Pad Prism 8 and statistical tests used are indicated in the figure legends and experimental model and subject details.

References Methods

44. Locci, M. *et al.* Human circulating PD-1+CXCR3-CXCR5+ memory Tfh cells are highly functional and correlate with broadly neutralizing HIV antibody responses. *Immunity* **39**, 758–769 (2013).
45. Juneja, V. R. *et al.* PD-L1 on tumor cells is sufficient for immune evasion in immunogenic tumors and inhibits CD8 T cell cytotoxicity. *J. Exp. Med.* **214**, 895–904 (2017).
46. Webster, K. E. *et al.* In vivo expansion of t reg cells with il-2-mab complexes: induction of resistance to eae and long-term acceptance of islet allografts without immunosuppression. *J. Exp. Med.* **206**, 751–760 (2009).
47. Ganesan, A. P. *et al.* Tissue-resident memory features are linked to the magnitude of cytotoxic T cell responses in human lung

cancer. *Nat. Immunol.* **18**, 940–950 (2017).

48. Singh, D. *et al.* CD4+ follicular helper-like T cells are key players in anti-tumor immunity. *bioRxiv* 2020.01.08.898346 (2020) doi:10.1101/2020.01.08.898346.

49. Engel, I. *et al.* Innate-like functions of natural killer T cell subsets result from highly divergent gene programs. *Nat. Immunol.* **17**, 728–739 (2016).

50. Picelli, S. *et al.* Full-length RNA-seq from single cells using Smart-seq2. *Nat. Protoc.* **9**, 171–181 (2014).

51. Trapnell, C., Pachter, L. & Salzberg, S. L. TopHat: discovering splice junctions with RNA-Seq. *Bioinformatics* **25**, 1105–1111 (2009).

52. Langmead, B., Trapnell, C., Pop, M. & Salzberg, S. L. Ultrafast and memory-efficient alignment of short DNA sequences to the human genome. *Genome Biol.* **10**, R25 (2009).

53. Li, H. & Durbin, R. Fast and accurate short read alignment with Burrows-Wheeler transform. *Bioinformatics* **25**, 1754–1760 (2009).

54. Anders, S., Pyl, P. T. & Huber, W. HTSeq--a Python framework to work with high-throughput sequencing data. *Bioinformatics* **31**, 166–169 (2015).

55. Bolger, A. M., Lohse, M. & Usadel, B. Trimmomatic: a flexible trimmer for Illumina sequence data. *Bioinformatics* **30**, 2114–2120 (2014).

56. Love, M. I., Huber, W. & Anders, S. Moderated estimation of fold change and dispersion for RNA-seq data with DESeq2. *Genome Biol.* **15**, 550 (2014).

57. Patil, V. S. *et al.* Precursors of human CD4 + cytotoxic T lymphocytes identified by single-cell transcriptome analysis. *Sci. Immunol.* **3**, 8664 (2018).

58. Ganesan, A.-P. *et al.* Tissue-resident memory features are linked to the magnitude of cytotoxic T cell responses in human lung cancer. *Nat. Immunol.* **18**, 940–950 (2017).

59. Langfelder, P. & Horvath, S. WGCNA: an R package for weighted correlation network analysis. *BMC Bioinformatics* **9**, 559 (2008).

60. Mellone, M. *et al.* Induction of fibroblast senescence generates a non-fibrogenic myofibroblast phenotype that differentially impacts on cancer prognosis. *Aging (Albany. NY).* **9**, 114–132 (2016).

61. Ottensmeier, C. H. *et al.* Upregulated Glucose Metabolism Correlates Inversely with CD8 $^{+}$ T-cell Infiltration and Survival in Squamous Cell Carcinoma. *Cancer Res.* **76**, 4136–4148 (2016).

62. Zheng, C. *et al.* Landscape of Infiltrating T Cells in Liver Cancer Revealed by Single-Cell Sequencing Resource Landscape of

Infiltrating T Cells in Liver Cancer Revealed by Single-Cell Sequencing. *Cell* **169**, 1342-1356.e16 (2017).

63. Zhang, L. *et al.* Lineage tracking reveals dynamic relationships of T cells in colorectal cancer. *Nature* **564**, 268–272 (2018).

64. Savas, P. *et al.* Single-cell profiling of breast cancer T cells reveals a tissue-resident memory subset associated with improved prognosis. *Nat. Med.* **24**, 986–993 (2018).

65. Lambrechts, D. *et al.* Phenotype molding of stromal cells in the lung tumor microenvironment. *Nat. Med.* **24**, 1277–1289 (2018).

66. Puram, S. V. *et al.* Single-Cell Transcriptomic Analysis of Primary and Metastatic Tumor Ecosystems in Head and Neck Cancer. *Cell* **171**, 1611-1624.e24 (2017).

67. Jerby-Arnon, L. *et al.* A Cancer Cell Program Promotes T Cell Exclusion and Resistance to Checkpoint Blockade. *Cell* **175**, 984-997.e24 (2018).

68. Li, H. *et al.* Dysfunctional CD8 T Cells Form a Proliferative, Dynamically Regulated Compartment within Human Melanoma. *Cell* **176**, 775-789.e18 (2019).

69. Stuart, T. *et al.* Comprehensive Integration of Single-Cell Data. *Cell* **177**, 1888-1902.e21 (2019).

70. Finak, G. *et al.* MAST: A flexible statistical framework for assessing transcriptional changes and characterizing heterogeneity in single-cell RNA sequencing data. *Genome Biol.* **16**, 278 (2015).

71. Kharchenko, P. V., Silberstein, L. & Scadden, D. T. Bayesian approach to single-cell differential expression analysis. *Nat. Methods* **11**, 740–742 (2014).

72. Trapnell, C. *et al.* The dynamics and regulators of cell fate decisions are revealed by pseudotemporal ordering of single cells. *Nat. Biotechnol.* **32**, 381–386 (2014).

73. Meckiff, B. J. *et al.* Imbalance of Regulatory and Cytotoxic SARS-CoV-2-Reactive $CD4^+$ T Cells in COVID-19. *Cell*, **183**, 1340-1353 (2020)

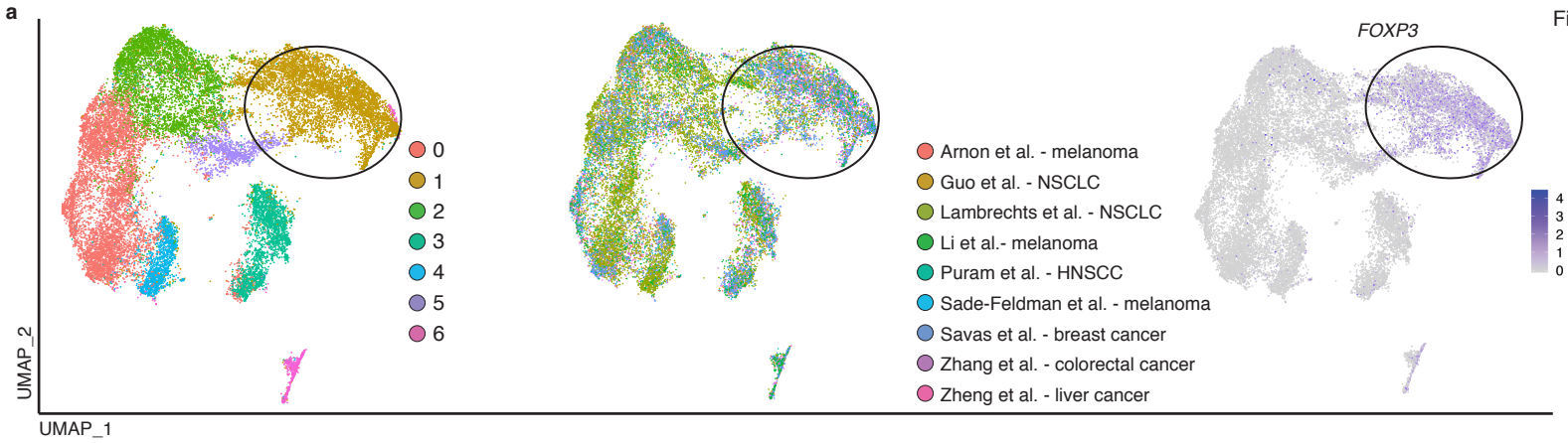
a
FOXP3
0
1
2
3
4
5
6
Arnon et al. - melanoma
Guo et al. - NSCLC
Lambrechts et al. - NSCLC
Li et al.- melanoma
Puram et al. - HNSCC
Sade-Feldman et al. - melanoma
Savas et al. - breast cancer
Zhang et al. - colorectal cancer
Zheng et al. - liver cancer
4
3
2
1
0
UMAP_2
UMAP_1

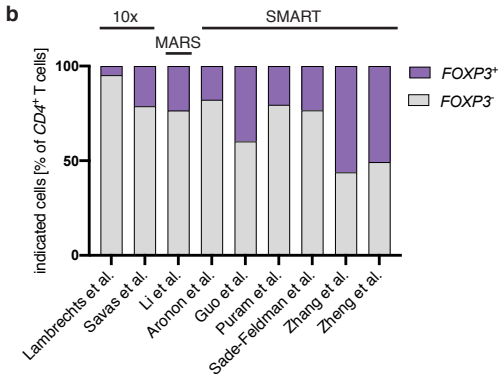
b
10x
SMART
MARS
indicated cells [% of CD4+ T cells]
100
50
0
FOXP3+
FOXP3-
Lambrechts et al.
Savas et al.
Li et al.
Aronon et al.
Guo et al.
Puram et al.
Sade-Feldman et al.
Zhang et al.
Zheng et al.

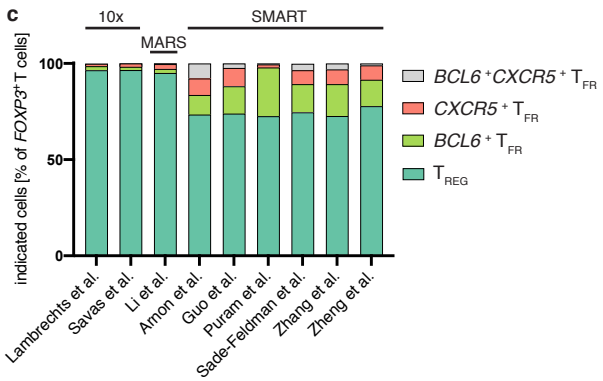
c
10x
SMART
MARS
indicated cells [% of FOXP3+ T cells]
100
50
0
BCL6+CXCR5+ TFR
CXCR5+ TFR
BCL6+ TFR
TREG
Lambrechts et al.
Savas et al.
Li et al.
Arnon et al.
Guo et al.
Puram et al.
Sade-Feldman et al.
Zhang et al.
Zheng et al.

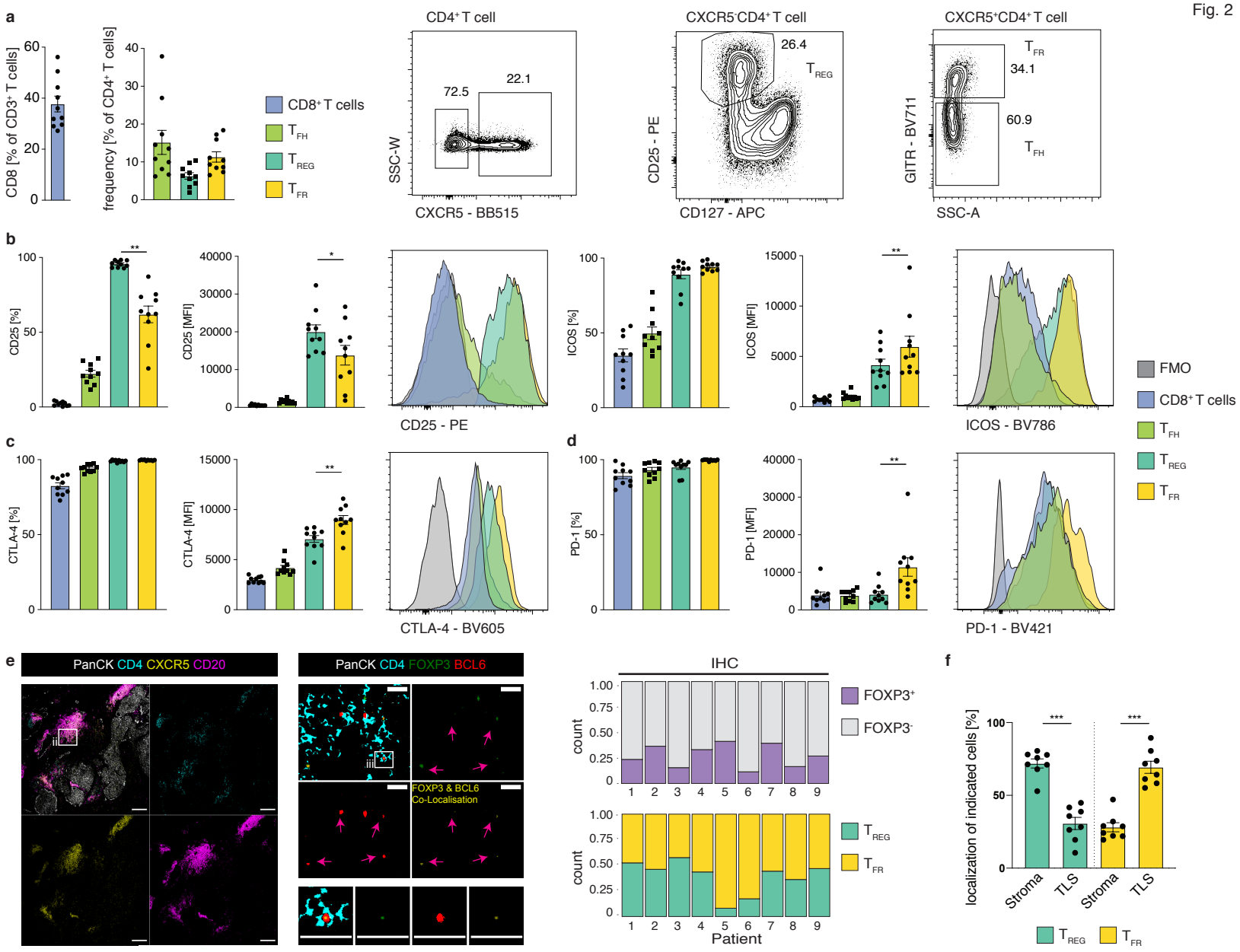
a
CD8 [% of CD3+ T cells]
frequency [% of CD4+ T cells]
CD8+ T cells
TFH
TREG
TFR
CD4+ T cell
SSC-W
CXCR5 - BB515
72.5
22.1
CXCR5-CD4+ T cell
CD25 - PE
CD127 - APC
26.4
TREG
CXCR5+CD4+ T cell
GITR - BV711
SSC-A
TFR
34.1
60.9
TFH
b
CD25 [%]
CD25 [MFI]
CD25 - PE
ICOS [%]
ICOS [MFI]
ICOS - BV786
FMO
CD8+ T cells
TFH
TREG
TFR
c
CTLA-4 [%]
CTLA-4 [MFI]
CTLA-4 - BV605
d
PD-1 [%]
PD-1 [MFI]
PD-1 - BV421
e
PanCK CD4 CXCR5 CD20
PanCK CD4 FOXP3 BCL6
FOXP3 & BCL6
Co-Localisation
IHC
count
FOXP3+
FOXP3-
TREG
TFR
Patient
f
localization of indicated cells [%]
Stroma
TLS
Stroma
TLS
TREG
TFR

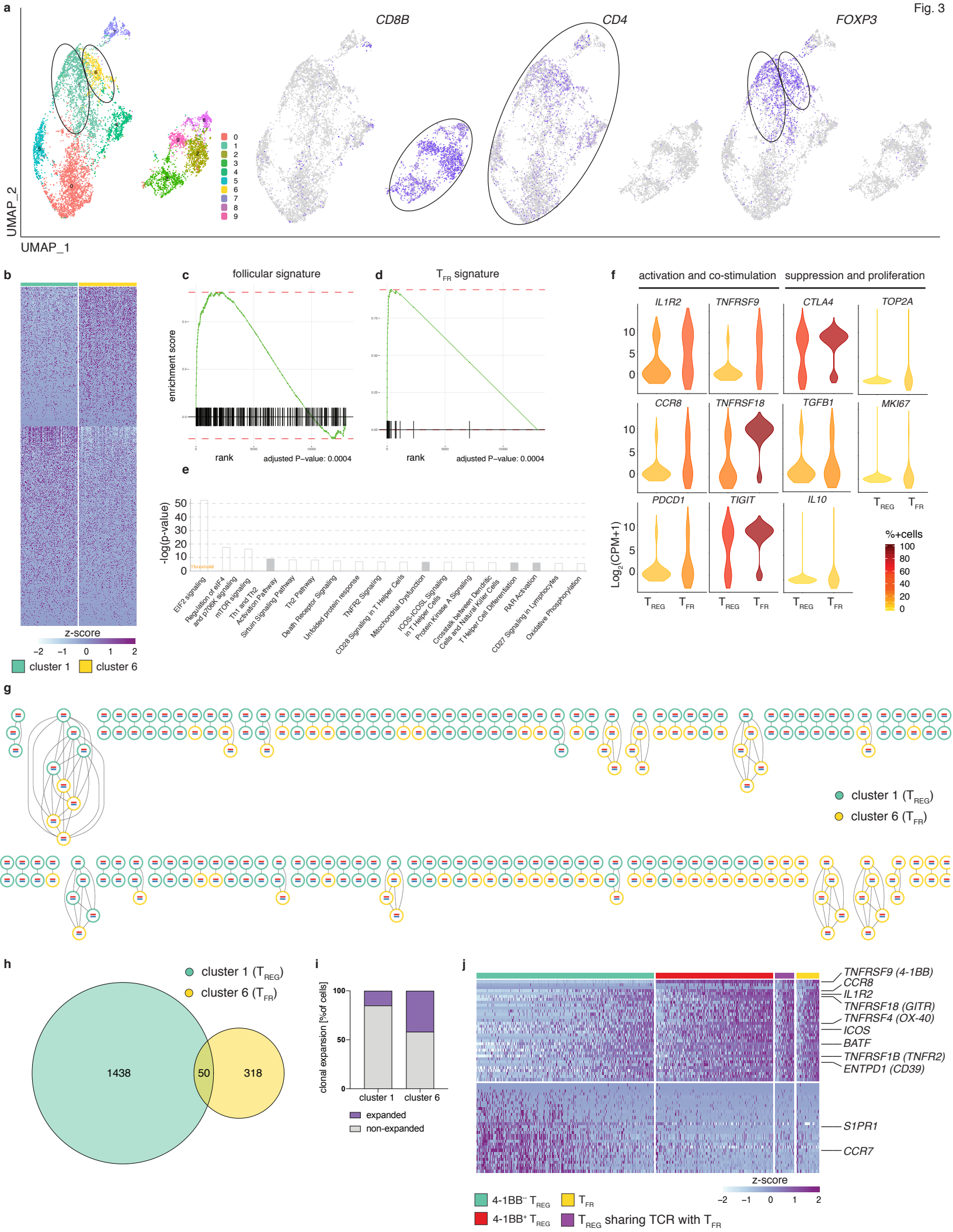
a
CD8B
CD4
FOXP3
UMAP_2
UMAP_1
0
1
2
3
4
5
6
7
8
9
b
z-score
−2 −1 0 1 2
cluster 1
cluster 6
c
follicular signature
enrichment score
rank
adjusted P−value: 0.0004
d
T_FR signature
rank
adjusted P−value: 0.0004
e
-log(p-value)
Threshold
EIF2 signaling
Regulation of eIF4 and p70S6K signaling
mTOR signaling
Th1 and Th2 Activation Pathway
Sirtuin Signaling Pathway
Th2 Pathway
Death Receptor Signaling
Unfolded protein response
TNFR2 Signaling
CD28 Signaling in T Helper Cells
Mitochondrial Dysfunction
ICOS-ICOSL Signaling in T Helper Cells
Protein Kinase A Signaling
Crosstalk between Dendritic Cells and Natural Killer Cells
T Helper Cell Differentiation
RAR Activation
CD27 Signaling in Lymphocytes
Oxidative Phosphorylation
f
activation and co-stimulation
suppression and proliferation
IL1R2
TNFRSF9
CTLA4
TOP2A
CCR8
TNFRSF18
TGFB1
MKI67
PDCD1
TIGIT
IL10
Log2(CPM+1)
T_REG
T_FR
%+cells
100
80
60
40
20
0
g
cluster 1 (T_REG)
cluster 6 (T_FR)
h
cluster 1 (T_REG)
cluster 6 (T_FR)
1438
50
318
i
clonal expansion [%of cells]
cluster 1
cluster 6
expanded
non-expanded
j
TNFRSF9 (4-1BB)
CCR8
IL1R2
TNFRSF18 (GITR)
TNFRSF4 (OX-40)
ICOS
BATF
TNFRSF1B (TNFR2)
ENTPD1 (CD39)
S1PR1
CCR7
z-score
−2 −1 0 1 2
4-1BB⁻ T_REG
T_FR
4-1BB⁺ T_REG
T_REG sharing TCR with T_FR

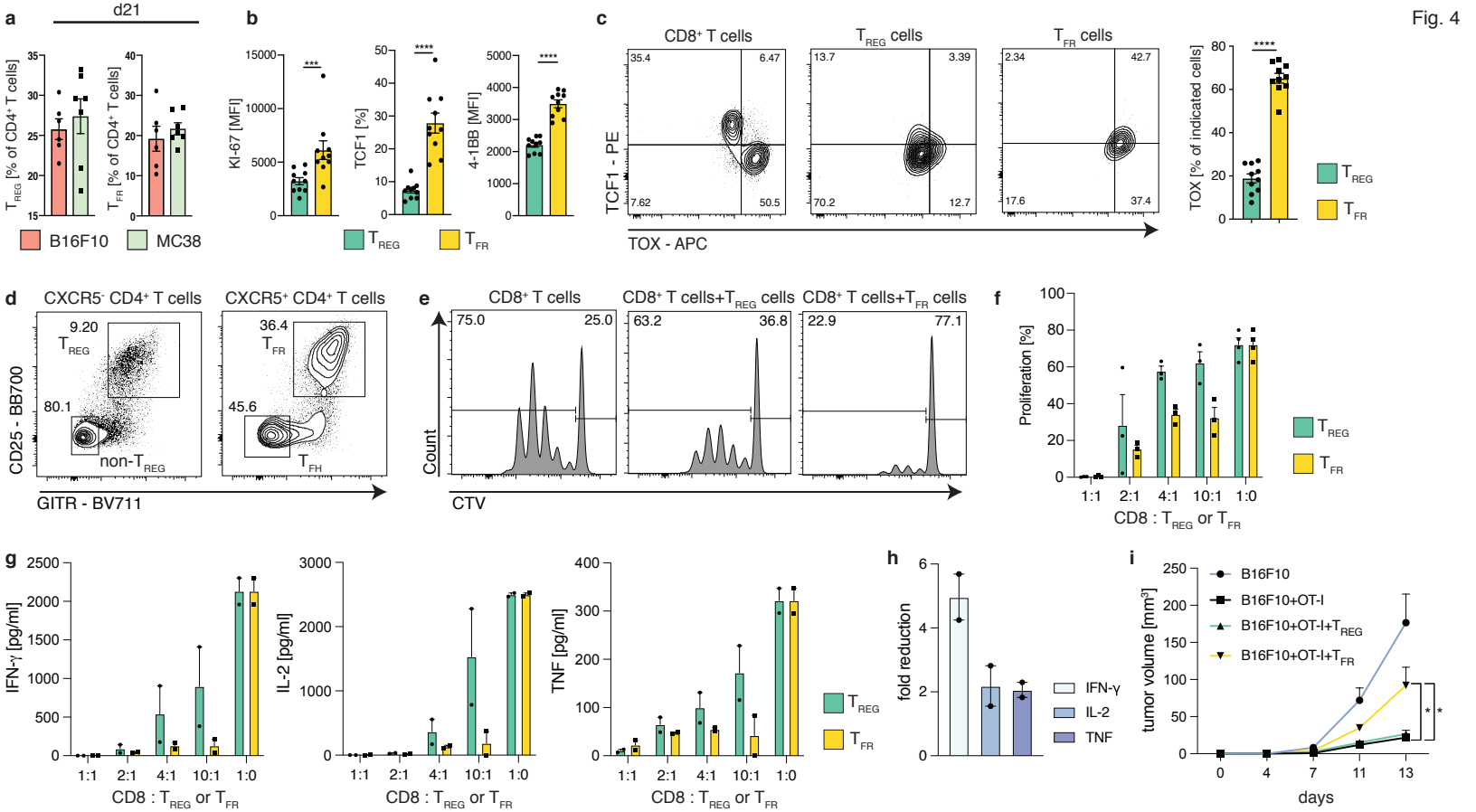
a
d21
TREG [% of CD4+ T cells]
TFR [% of CD4+ T cells]
B16F10
MC38
b
KI-67 [MFI]
TCF1 [%]
4-1BB [MFI]
***
****
****
TREG
TFR
c
CD8+ T cells
TREG cells
TFR cells
TCF1 - PE
TOX - APC
35.4
6.47
7.62
50.5
13.7
3.39
70.2
12.7
2.34
42.7
17.6
37.4
TOX [% of indicated cells]
****
TREG
TFR
d
CXCR5- CD4+ T cells
CXCR5+ CD4+ T cells
CD25 - BB700
GITR - BV711
9.20
TREG
80.1
non-TREG
36.4
TFR
45.6
TFH
e
CD8+ T cells
CD8+ T cells+TREG cells
CD8+ T cells+TFR cells
Count
CTV
75.0
25.0
63.2
36.8
22.9
77.1
f
Proliferation [%]
CD8 : TREG or TFR
1:1
2:1
4:1
10:1
1:0
TREG
TFR
g
IFN-γ [pg/ml]
IL-2 [pg/ml]
TNF [pg/ml]
CD8 : TREG or TFR
TREG
TFR
h
fold reduction
IFN-γ
IL-2
TNF
i
tumor volume [mm3]
B16F10
B16F10+OT-I
B16F10+OT-I+TREG
B16F10+OT-I+TFR
days
**

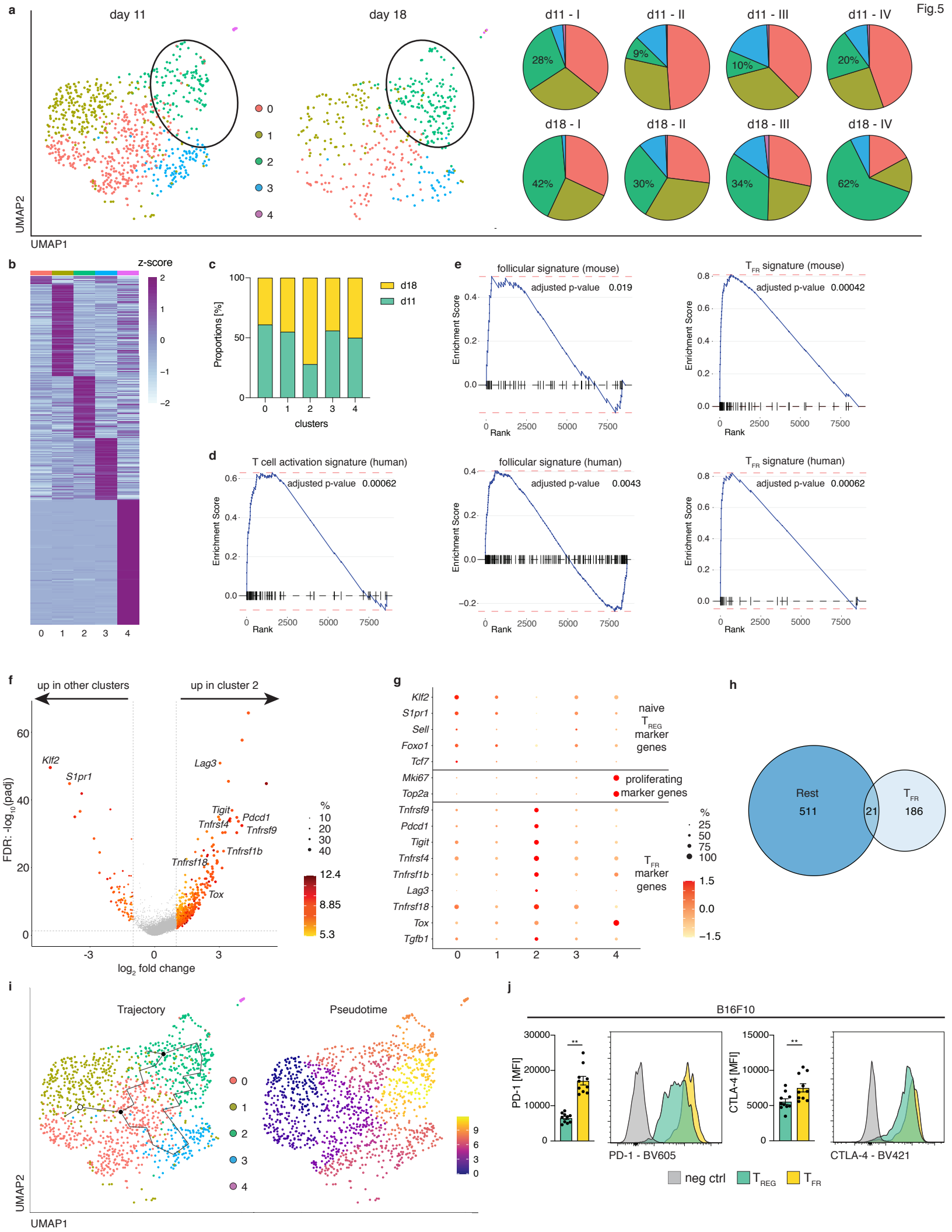
a
day 11
day 18
UMAP2
UMAP1
0
1
2
3
4
d11 - I
d11 - II
d11 - III
d11 - IV
d18 - I
d18 - II
d18 - III
d18 - IV
28%
9%
10%
20%
42%
30%
34%
62%
b
z-score
2
1
0
−1
−2
0 1 2 3 4
c
Proportions [%]
clusters
d18
d11
d
T cell activation signature (human)
adjusted p-value 0.00062
Enrichment Score
Rank
e
follicular signature (mouse)
adjusted p-value 0.019
T_FR signature (mouse)
adjusted p-value 0.00042
follicular signature (human)
adjusted p-value 0.0043
T_FR signature (human)
adjusted p-value 0.00062
f
up in other clusters
up in cluster 2
FDR: -log10(padj)
log2 fold change
Klf2
S1pr1
Lag3
Tigit
Pdcd1
Tnfrsf4
Tnfrsf9
Tnfrsf1b
Tnfrsf18
Tox
%
10
20
30
40
12.4
8.85
5.3
g
Klf2
S1pr1
Sell
Foxo1
Tcf7
naive T_REG marker genes
Mki67
Top2a
proliferating marker genes
Tnfrsf9
Pdcd1
Tigit
Tnfrsf4
Tnfrsf1b
Lag3
Tnfrsf18
Tox
Tgfb1
T_FR marker genes
%
25
50
75
100
1.5
0.0
−1.5
h
Rest
511
21
T_FR
186
i
Trajectory
Pseudotime
UMAP2
UMAP1
j
B16F10
PD-1 [MFI]
PD-1 - BV605
CTLA-4 [MFI]
CTLA-4 - BV421
neg ctrl
T_REG
T_FR

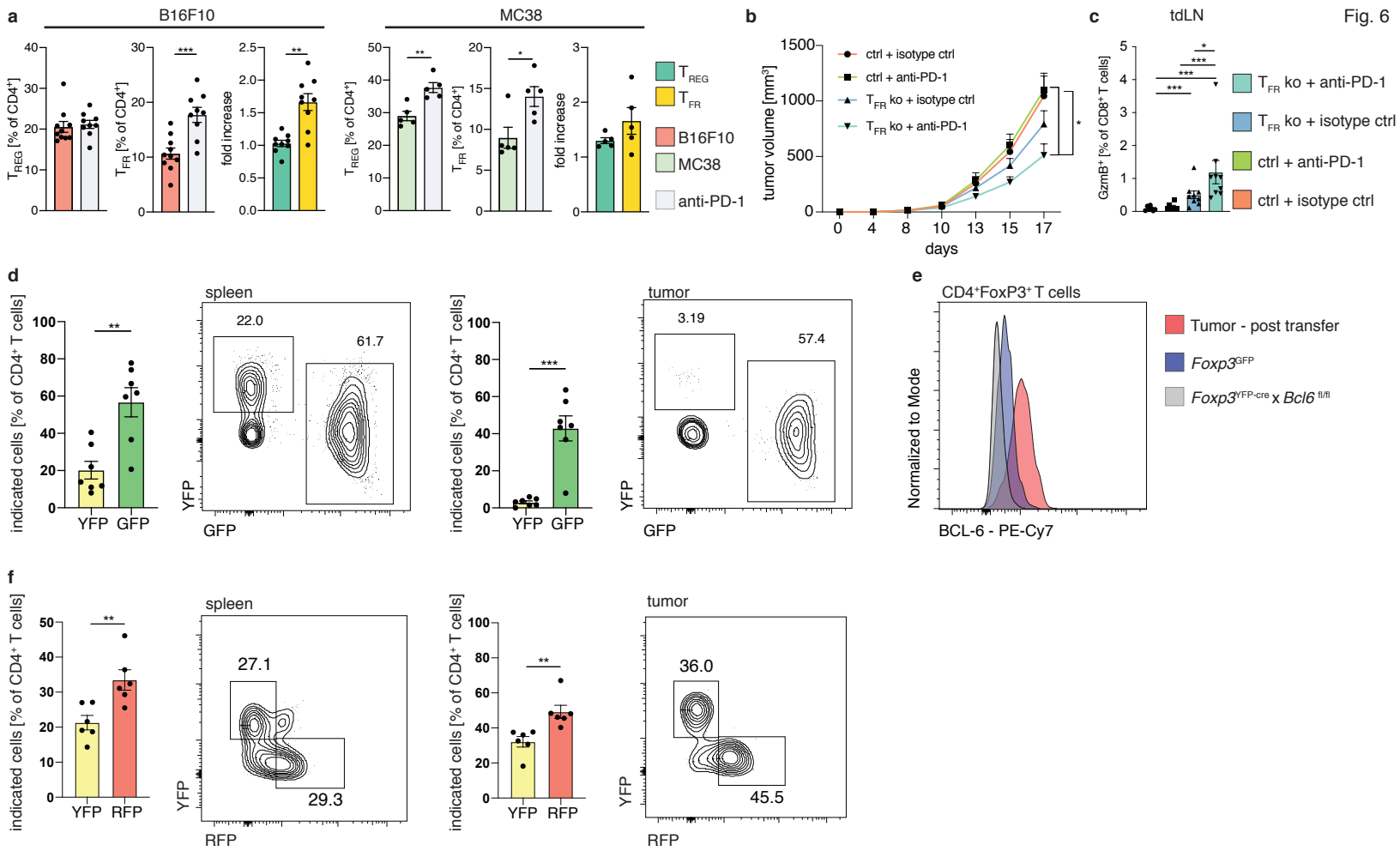
a
B16F10
MC38
T_REG [% of CD4+]
T_FR [% of CD4+]
fold increase
T_REG
T_FR
B16F10
MC38
anti-PD-1
b
tumor volume [mm3]
ctrl + isotype ctrl
ctrl + anti-PD-1
T_FR ko + isotype ctrl
T_FR ko + anti-PD-1
days
c
tdLN
GzmB+ [% of CD8+ T cells]
T_FR ko + anti-PD-1
T_FR ko + isotype ctrl
ctrl + anti-PD-1
ctrl + isotype ctrl
d
spleen
tumor
indicated cells [% of CD4+ T cells]
YFP
GFP
22.0
61.7
3.19
57.4
e
CD4+FoxP3+ T cells
Normalized to Mode
BCL-6 - PE-Cy7
Tumor - post transfer
Foxp3GFP
Foxp3YFP-cre x Bcl6 fl/fl
f
spleen
tumor
indicated cells [% of CD4+ T cells]
YFP
RFP
27.1
29.3
36.0
45.5

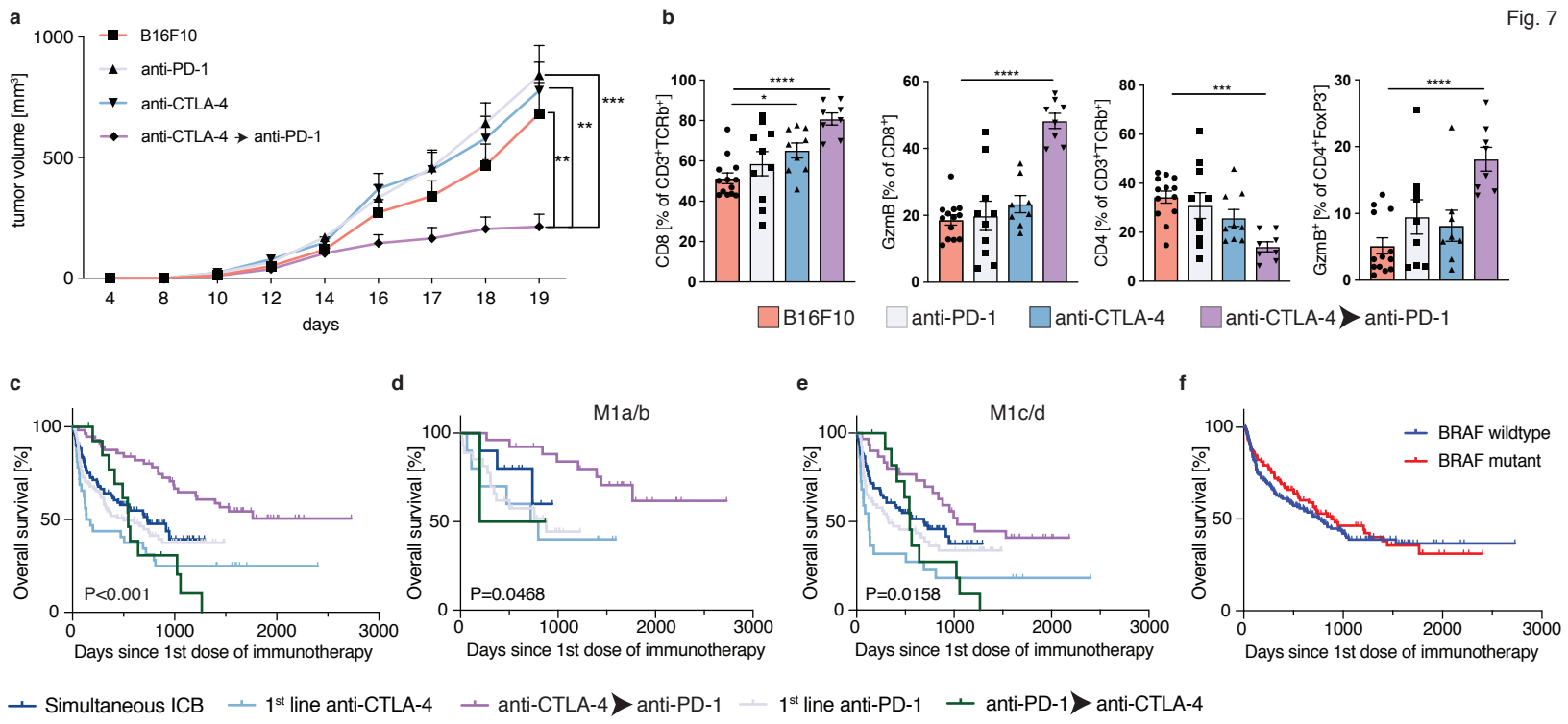
a
tumor volume [mm³]
B16F10
anti-PD-1
anti-CTLA-4
anti-CTLA-4 ➝ anti-PD-1
days
b
CD8 [% of CD3⁺TCRb⁺]
GzmB [% of CD8⁺]
CD4 [% of CD3⁺TCRb⁺]
GzmB⁺ [% of CD4⁺FoxP3⁺]
B16F10
anti-PD-1
anti-CTLA-4
anti-CTLA-4 ➤ anti-PD-1

c
Overall survival [%]
P<0.001
Days since 1st dose of immunotherapy
d
M1a/b
P=0.0468
e
M1c/d
P=0.0158
f
BRAF wildtype
BRAF mutant
Simultaneous ICB
1st line anti-CTLA-4
anti-CTLA-4 ➤ anti-PD-1
1st line anti-PD-1
anti-PD-1 ➤ anti-CTLA-4

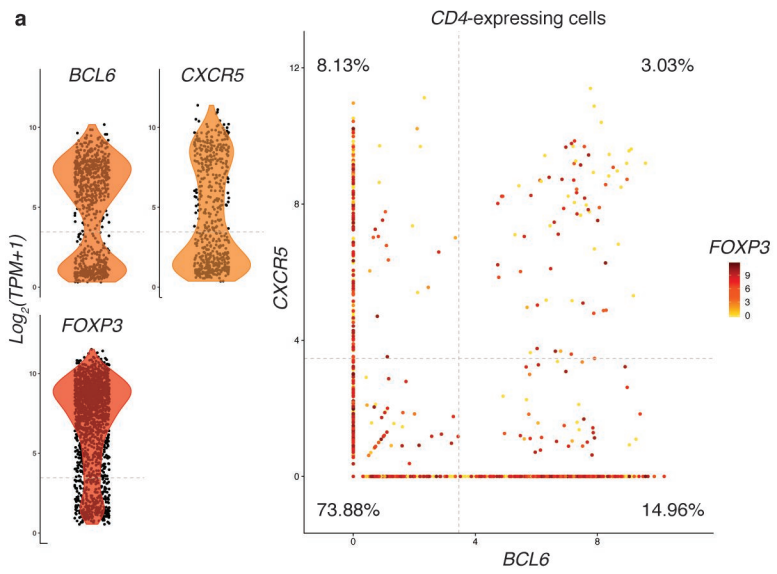
a
CD4-expressing cells
BCL6
CXCR5
FOXP3
Log2(TPM+1)
8.13%
3.03%
73.88%
14.96%
CXCR5
BCL6
FOXP3

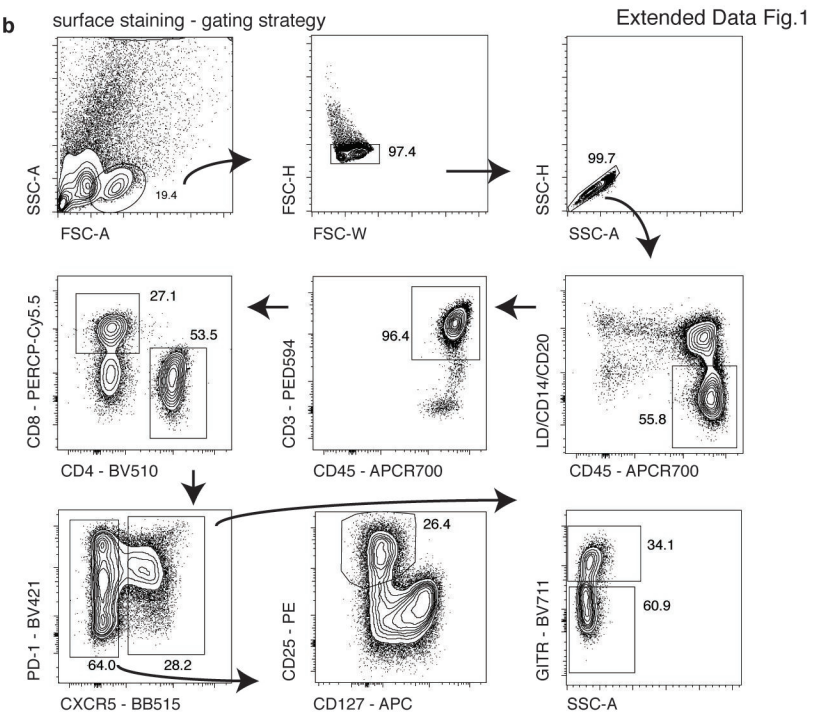
b
surface staining - gating strategy
SSC-A
FSC-A
19.4
FSC-H
FSC-W
97.4
SSC-H
SSC-A
99.7
CD8 - PERCP-Cy5.5
CD4 - BV510
27.1
53.5
CD3 - PED594
CD45 - APCR700
96.4
LD/CD14/CD20
CD45 - APCR700
55.8
PD-1 - BV421
CXCR5 - BB515
64.0
28.2
CD25 - PE
CD127 - APC
26.4
GITR - BV711
SSC-A
34.1
60.9

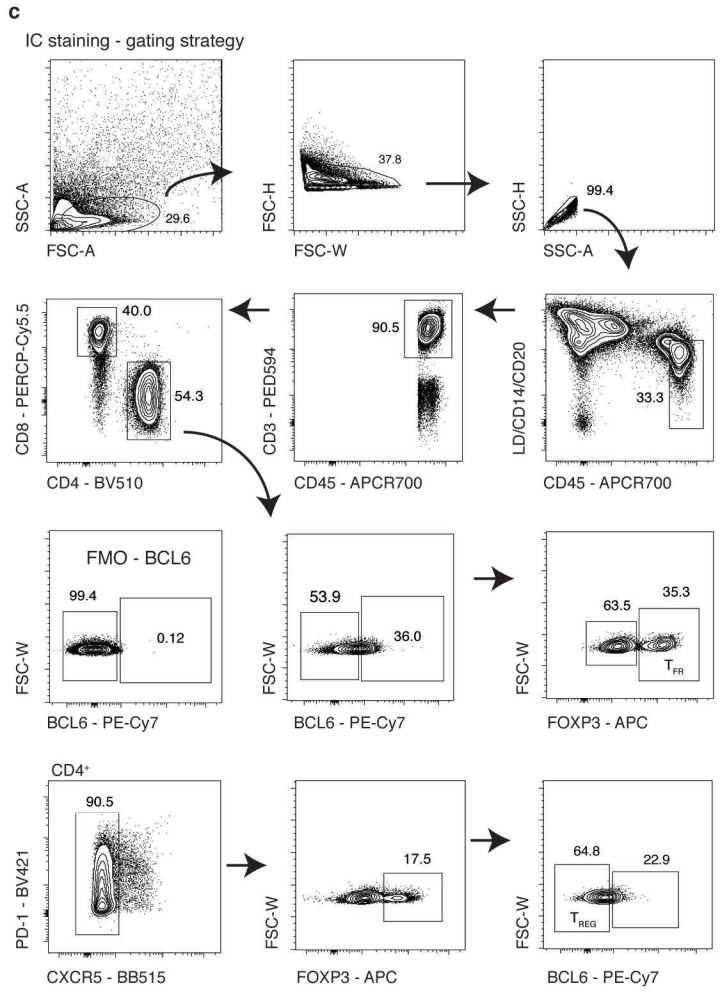
c
IC staining - gating strategy
SSC-A
FSC-A
29.6
FSC-H
FSC-W
37.8
SSC-H
SSC-A
99.4
CD8 - PERCP-Cy5.5
CD4 - BV510
40.0
54.3
CD3 - PED594
CD45 - APCR700
90.5
LD/CD14/CD20
CD45 - APCR700
33.3
FMO - BCL6
FSC-W
BCL6 - PE-Cy7
99.4
0.12
FSC-W
BCL6 - PE-Cy7
53.9
36.0
FSC-W
FOXP3 - APC
63.5
35.3
T FR
CD4+
PD-1 - BV421
CXCR5 - BB515
90.5
FSC-W
FOXP3 - APC
17.5
FSC-W
BCL6 - PE-Cy7
64.8
22.9
T REG

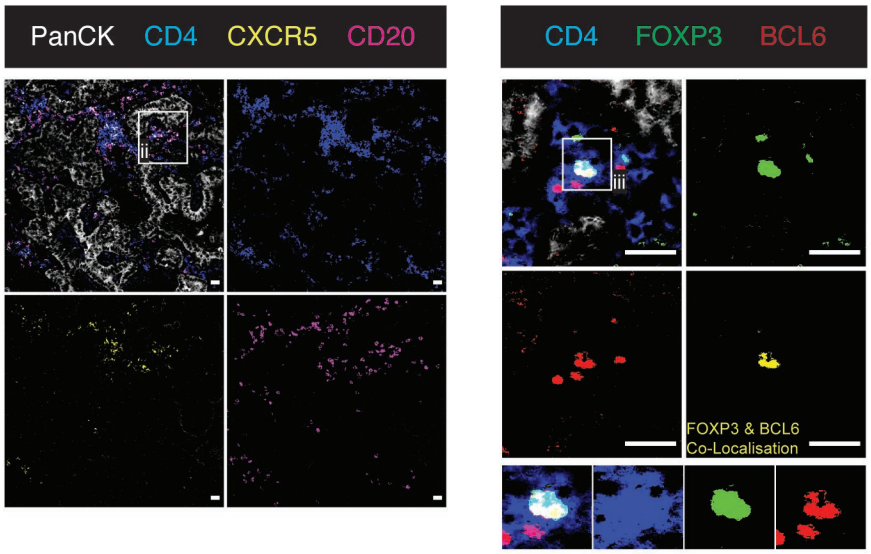
d
PanCK
CD4
CXCR5
CD20
ii
CD4
FOXP3
BCL6
iii
FOXP3 & BCL6
Co-Localisation

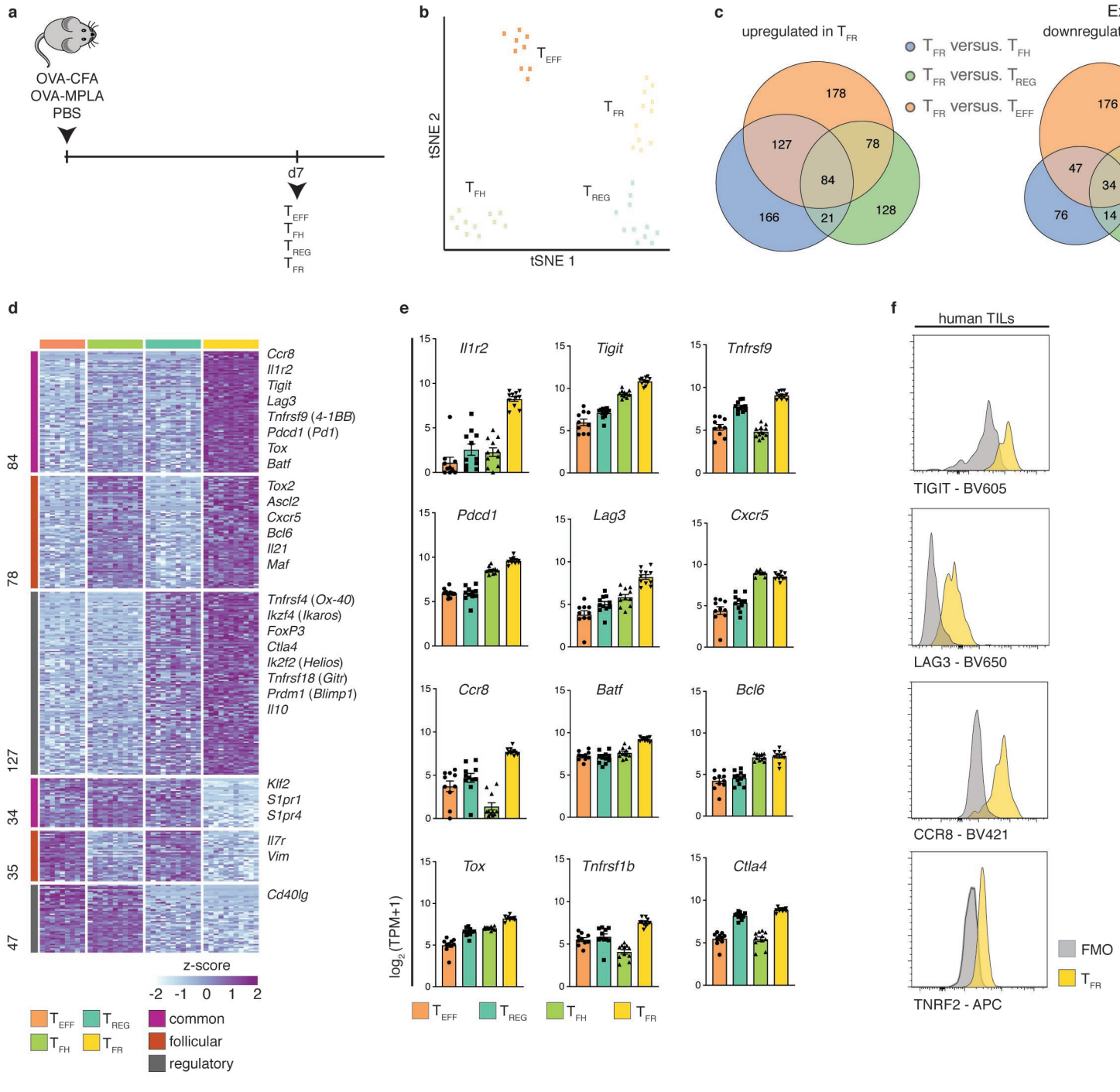
a
OVA-CFA
OVA-MPLA
PBS
d7
T_{EFF}
T_{FH}
T_{REG}
T_{FR}
b
tSNE 2
tSNE 1
c
upregulated in T_{FR}
downregulated in T_{FR}
T_{FR} versus. T_{FH}
T_{FR} versus. T_{REG}
T_{FR} versus. T_{EFF}
178
127
78
84
166
21
128
176
47
35
34
76
14
148
d
84
78
127
34
35
47
Ccr8
Il1r2
Tigit
Lag3
Tnfrsf9 (4-1BB)
Pdcd1 (Pd1)
Tox
Batf
Tox2
Ascl2
Cxcr5
Bcl6
Il21
Maf
Tnfrsf4 (Ox-40)
Ikzf4 (Ikaros)
FoxP3
Ctla4
Ik2f2 (Helios)
Tnfrsf18 (Gitr)
Prdm1 (Blimp1)
Il10
Klf2
S1pr1
S1pr4
Il7r
Vim
Cd40lg
z-score
-2 -1 0 1 2
T_{EFF} T_{REG} common
T_{FH} T_{FR} follicular
regulatory
e
Il1r2
Tigit
Tnfrsf9
Pdcd1
Lag3
Cxcr5
Ccr8
Batf
Bcl6
Tox
Tnfrsf1b
Ctla4
log_2(TPM+1)
T_{EFF} T_{REG} T_{FH} T_{FR}
f
human TILs
TIGIT - BV605
LAG3 - BV650
CCR8 - BV421
TNRF2 - APC
FMO
T_{FR}

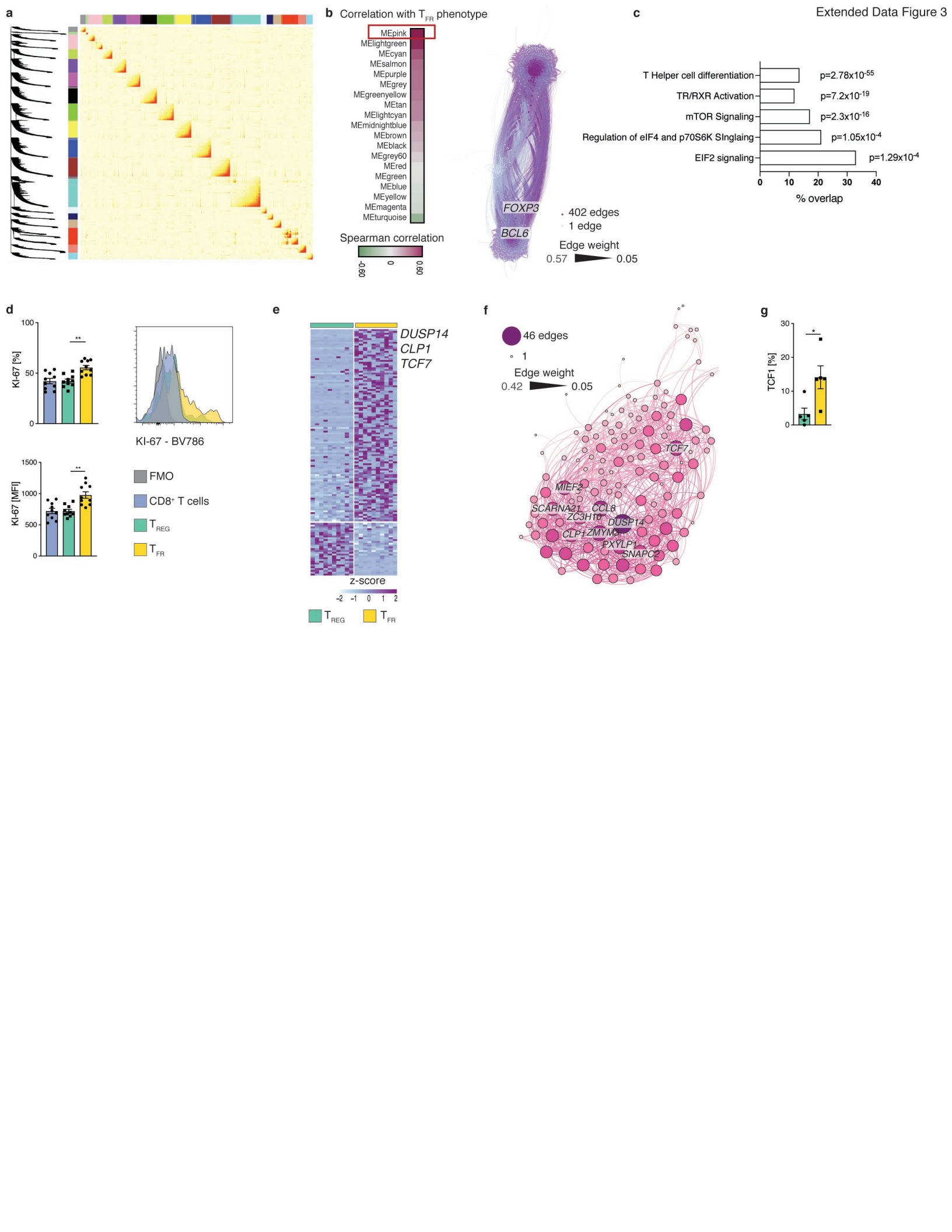
a
b
Correlation with T_{FR} phenotype
MEpink
MElightgreen
MEcyan
MEsalmon
MEpurple
MEgrey
MEgreenyellow
MEtan
MElightcyan
MEmidnightblue
MEbrown
MEblack
MEgrey60
MEred
MEgreen
MEblue
MEyellow
MEmagenta
MEturquoise
Spearman correlation
-0.60
0
0.60
FOXP3
BCL6
402 edges
1 edge
Edge weight
0.57
0.05
c
T Helper cell differentiation
p=2.78x10-55
TR/RXR Activation
p=7.2x10-19
mTOR Signaling
p=2.3x10-16
Regulation of eIF4 and p70S6K SInglaing
p=1.05x10-4
EIF2 signaling
p=1.29x10-4
0
10
20
30
40
% overlap
d
KI-67 [%]
100
50
0
**
KI-67 - BV786
KI-67 [MFI]
1500
1000
500
0
**
FMO
CD8+ T cells
T_{REG}
T_{FR}
e
DUSP14
CLP1
TCF7
z-score
-2
-1
0
1
2
T_{REG}
T_{FR}
f
46 edges
1
Edge weight
0.42
0.05
TCF7
MIEF2
SCARNA21
CCL8
ZC3H10
DUSP14
CLP1
ZMYM3
PXYLP1
SNAPC2
g
TCF1 [%]
30
20
10
0
*

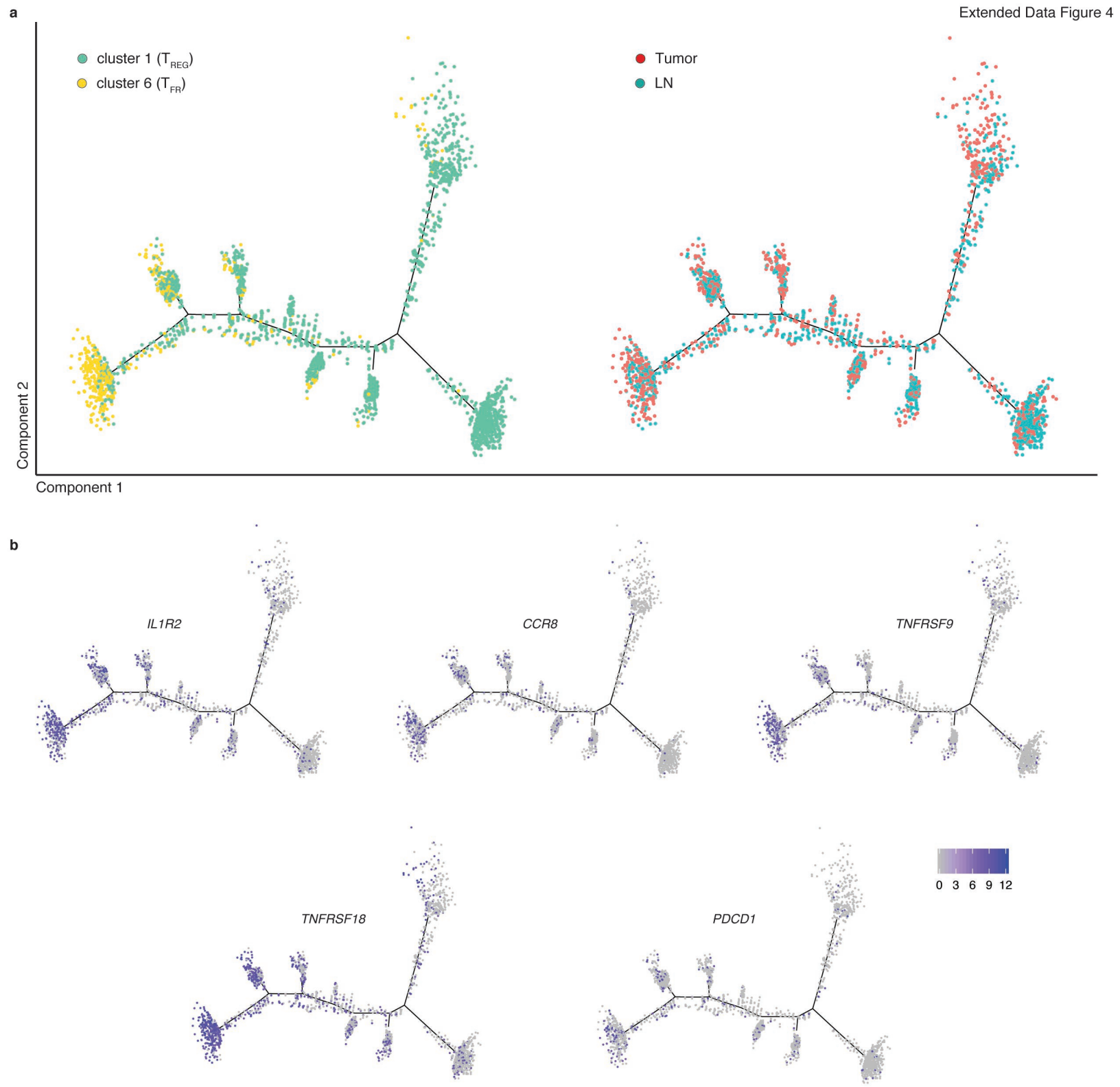
a
cluster 1 (T_{REG})
cluster 6 (T_{FR})
Tumor
LN
Component 2
Component 1
b
IL1R2
CCR8
TNFRSF9
TNFRSF18
PDCD1
0 3 6 9 12

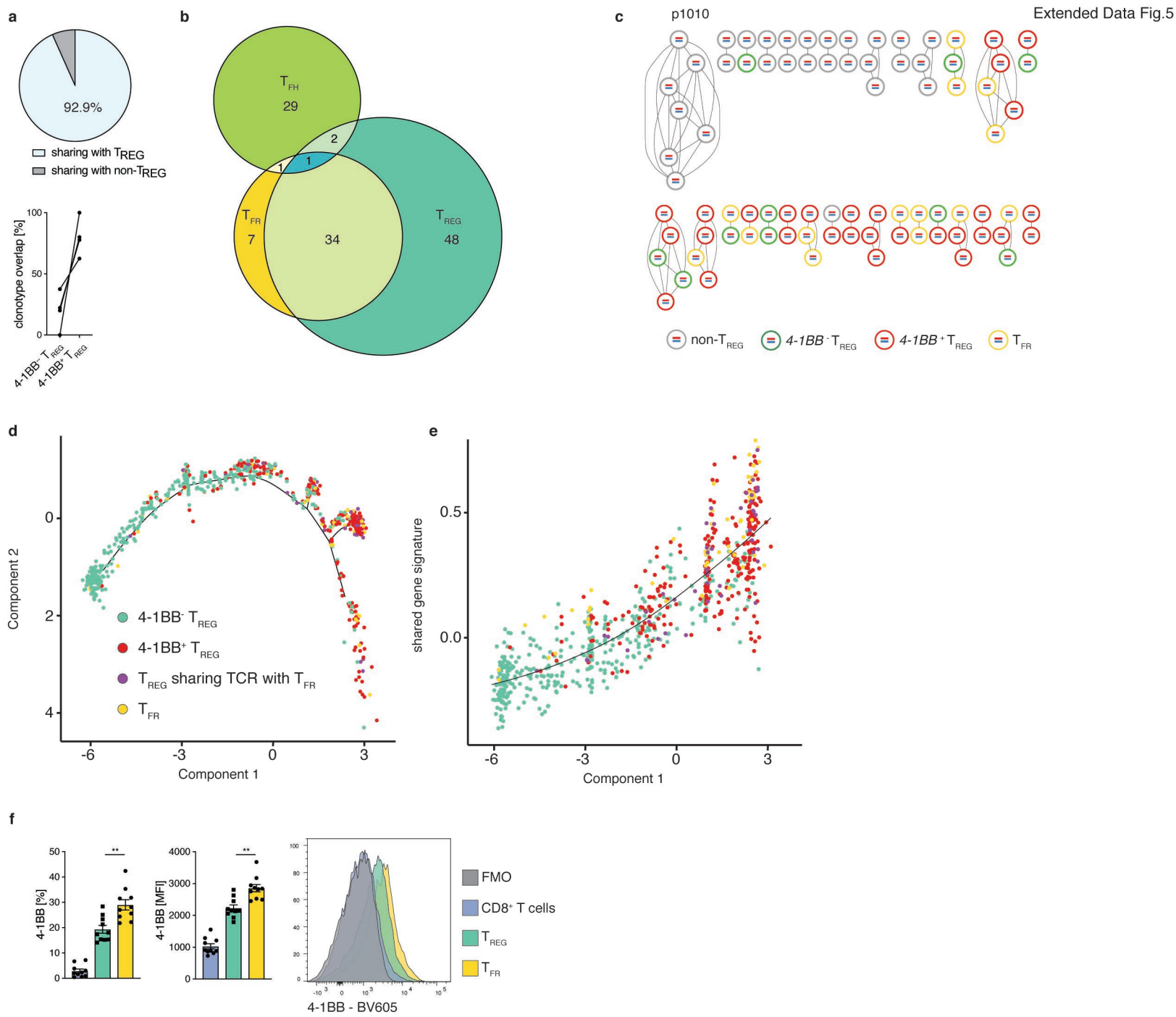
a
92.9%
sharing with TREG
sharing with non-TREG
clonotype overlap [%]
100
50
0
4-1BB- TREG
4-1BB+ TREG
b
TFH
29
2
1
1
TFR
7
34
TREG
48
c
p1010
non-TREG
4-1BB- TREG
4-1BB+ TREG
TFR
d
Component 2
0
2
4
-6
-3
0
3
Component 1
4-1BB- TREG
4-1BB+ TREG
TREG sharing TCR with TFR
TFR
e
shared gene signature
0.5
0.0
-6
-3
0
3
Component 1

f
4-1BB [%]
50
40
30
20
10
0
**
4-1BB [MFI]
4000
3000
2000
1000
0
**
4-1BB - BV605
FMO
CD8+ T cells
TREG
TFR

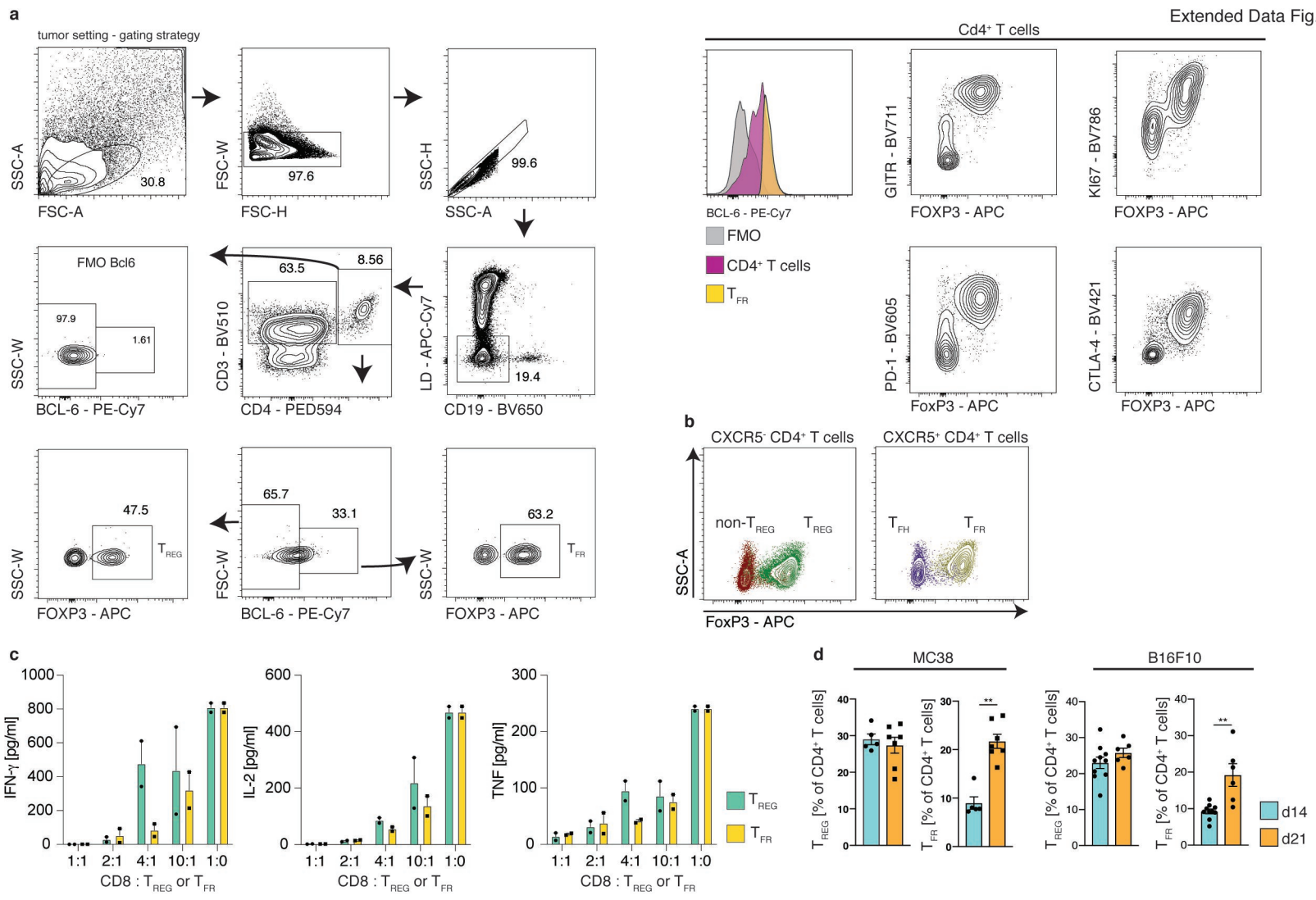
a
tumor setting - gating strategy
SSC-A
FSC-A
30.8
FSC-W
FSC-H
97.6
SSC-H
SSC-A
99.6
FMO Bcl6
SSC-W
BCL-6 - PE-Cy7
97.9
1.61
CD3 - BV510
CD4 - PED594
63.5
8.56
LD - APC-Cy7
CD19 - BV650
19.4
SSC-W
FOXP3 - APC
47.5
T_REG
FSC-W
BCL-6 - PE-Cy7
65.7
33.1
SSC-W
FOXP3 - APC
63.2
T_FR
Cd4+ T cells
BCL-6 - PE-Cy7
FMO
CD4+ T cells
T_FR
GITR - BV711
FOXP3 - APC
KI67 - BV786
FOXP3 - APC
PD-1 - BV605
FoxP3 - APC
CTLA-4 - BV421
FOXP3 - APC
b
CXCR5- CD4+ T cells
CXCR5+ CD4+ T cells
non-T_REG
T_REG
T_FH
T_FR
SSC-A
FoxP3 - APC

c
IFN-γ [pg/ml]
IL-2 [pg/ml]
TNF [pg/ml]
1:1
2:1
4:1
10:1
1:0
CD8 : T_REG or T_FR
T_REG
T_FR

d
MC38
B16F10
T_REG [% of CD4+ T cells]
T_FR [% of CD4+ T cells]
**
d14
d21

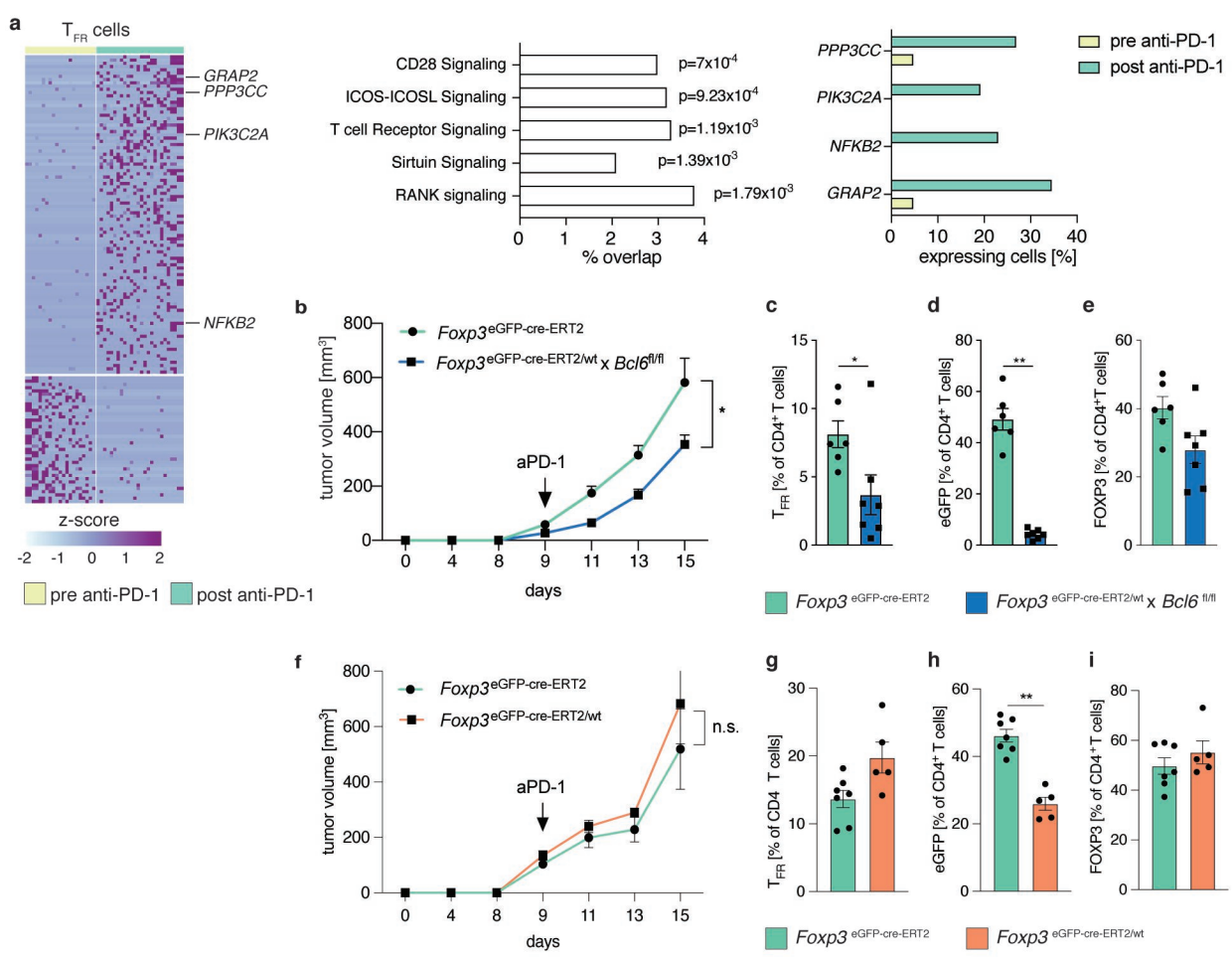
a
T FR cells
GRAP2
PPP3CC
PIK3C2A
NFKB2
z-score
-2 -1 0 1 2
pre anti-PD-1
post anti-PD-1
CD28 Signaling
ICOS-ICOSL Signaling
T cell Receptor Signaling
Sirtuin Signaling
RANK signaling
p=7x10-4
p=9.23x10-4
p=1.19x10-3
p=1.39x10-3
p=1.79x10-3
% overlap
PPP3CC
PIK3C2A
NFKB2
GRAP2
expressing cells [%]
b
Foxp3eGFP-cre-ERT2
Foxp3eGFP-cre-ERT2/wt x Bcl6fl/fl
tumor volume [mm3]
aPD-1
days
c
TFR [% of CD4+ T cells]
d
eGFP [% of CD4+ T cells]
e
FOXP3 [% of CD4+ T cells]
Foxp3 eGFP-cre-ERT2
Foxp3 eGFP-cre-ERT2/wt x Bcl6 fl/fl
f
Foxp3eGFP-cre-ERT2
Foxp3eGFP-cre-ERT2/wt
n.s.
tumor volume [mm3]
aPD-1
days
g
TFR [% of CD4 T cells]
h
eGFP [% of CD4+ T cells]
i
FOXP3 [% of CD4+ T cells]
Foxp3 eGFP-cre-ERT2
Foxp3 eGFP-cre-ERT2/wt

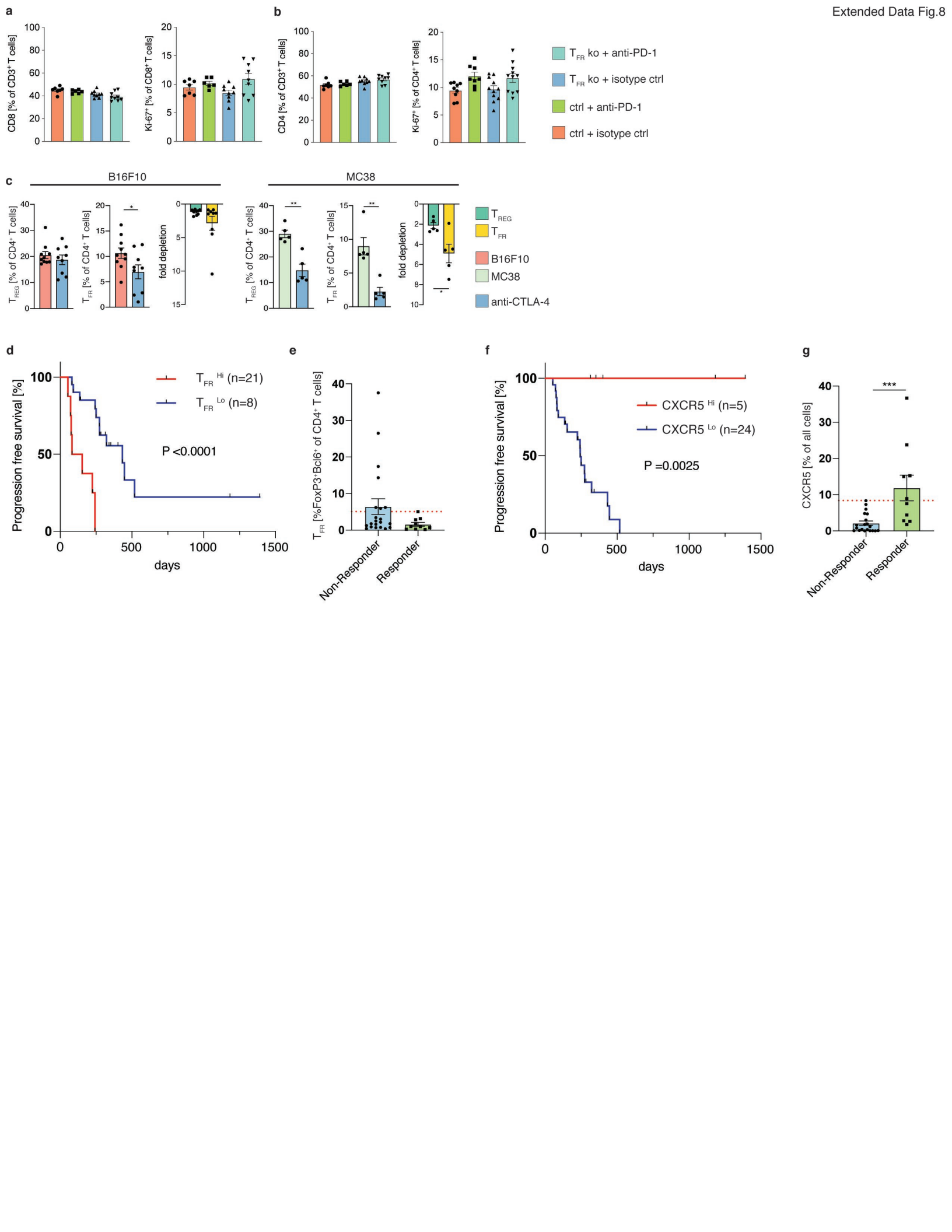
a
CD8 [% of CD3+ T cells]
Ki-67+ [% of CD8+ T cells]
b
CD4 [% of CD3+ T cells]
Ki-67+ [% of CD4+ T cells]
TFR ko + anti-PD-1
TFR ko + isotype ctrl
ctrl + anti-PD-1
ctrl + isotype ctrl
c
B16F10
MC38
TREG [% of CD4+ T cells]
TFR [% of CD4+ T cells]
fold depletion
TREG
TFR
B16F10
MC38
anti-CTLA-4
d
Progression free survival [%]
TFR Hi (n=21)
TFR Lo (n=8)
P <0.0001
days
e
TFR [%FoxP3+Bcl6+ of CD4+ T cells]
Non-Responder
Responder
f
Progression free survival [%]
CXCR5 Hi (n=5)
CXCR5 Lo (n=24)
P =0.0025
days
g
CXCR5 [% of all cells]
Non-Responder
Responder